

Off-stoichiometric effect on magnetic and electron transport properties of $\text{Fe}_2\text{VAl}_{1.35}$ in respect to Ni_2VAl ; Comparative study

A. Ślebarski,^{1,2,3} M. Fijałkowski,^{4,2} J. Deniszczyk,⁵ M. M. Maška,⁶ and D. Kaczorowski^{1,2}

¹*Institute of Low Temperature and Structure Research,
Polish Academy of Sciences, Okólna 2, 50-422 Wrocław, Poland*

²*Centre for Advanced Materials and Smart Structures,
Polish Academy of Sciences, Okólna 2, 50-422 Wrocław, Poland*

^{3*} *Author to whom correspondence should be addressed: andrzej.slebarski@us.edu.pl*

⁴*Institute of Physics, University of Silesia in Katowice, 75 Pułku Piechoty 1, 41-500 Chorzów, Poland*

⁵*Institute of Materials Engineering, University of Silesia in Katowice, 75 Pułku Piechoty 1A, 41-500 Chorzów, Poland*

⁶*Institute of Theoretical Physics, Wrocław University of Science and Technology,
Wybrzeże Wyspiańskiego 27, 50-370 Wrocław, Poland*

Density functional theory (DFT) calculations confirm that the structurally ordered Fe_2VAl Heusler alloy is nonmagnetic narrow-gap semiconductor. This compound is apt to form various disordered modifications with high concentration of antisite defects. We study the effect of structural disorder on the electronic structure, magnetic, and electronic transport properties of the full Heusler alloy Fe_2VAl and its off-stoichiometric equivalent $\text{Fe}_2\text{VAl}_{1.35}$. Data analysis in relation to *ab initio* calculations indicates an appearance of antisite disorder mainly due to Fe–V and Fe–Al stoichiometric variations. The data for weakly magnetic $\text{Fe}_2\text{VAl}_{1.35}$ are discussed in respect to Ni_2VAl . $\text{Fe}_2\text{VAl}_{1.35}$ can be classified as a nearly ferromagnetic metal with a pronounced spin glassy contribution, which, however, does not give a predominant effect on its thermoelectric properties. The figure of merit ZT is at 300 K about 0.05 for the Fe sample and 0.02 for Ni one, respectively. However, it is documented that the narrow d band resulting from Fe/V site exchange can be responsible for the unusual temperature dependencies of the physical properties of the $\text{Fe}_2\text{TiAl}_{1.35}$ alloy, characteristic of strongly correlated electron systems. As an example, the magnetic susceptibility of $\text{Fe}_2\text{VAl}_{1.35}$ exhibits singularity characteristic of a Griffiths phase, appearing as an inhomogeneous electronic state below $T_G \sim 200$ K. We also performed numerical analysis which supports the Griffiths phase scenario.

PACS numbers: 71.10.Hf, 71.20.Be, 71.20.-b, 71.27.+a, 75.20.Hr

I. INTRODUCTION

Cubic Heusler compounds, known as Heusler alloys, constitute a large family of materials, exhibiting a variety of interesting properties, both with respect to basic and applied investigations [1, 2]. In particular, in the last two decades, it has been experimentally demonstrated that some Heusler alloys can exhibit superconductivity [3] as well as topological effects [4], they are also promising materials for thermoelectric applications [5]. These alloys continue to be an active area of research in condensed matter physics. Particular attention is paid to examining the impact of a widely understood atomic disorder on the physical properties of these alloys. As an example, for a number of Fe-based Heusler alloys, disorder caused by dopants, off-stoichiometry of the system, or the presence of antisite (AS) Fe defects has been shown to enhance their thermoelectric properties [5], as well as it may give a reason for the appearance of exotic phenomena related to magnetic instabilities, which are in many cases associated with the proximity of a quantum critical point (QCP) [6, 7]. However, the origin of these behaviors is still controversial. A good example of such quantum phenomena seems to be Fe_2VAl . The investigations of the off-stoichiometric $\text{Fe}_{2+x}\text{V}_{1-x}\text{Al}$ and $\text{Fe}_2\text{VAl}_{1-x}$ equivalents have suggested the presence of a metal-insulator transition resulting in observed singu-

larities and enhancements of thermodynamic quantities near the expected ferromagnetic QCP [8, 9]. Fe_2VAl is a nonmagnetic and nonmetallic (semimetallic) material, exhibiting a narrow pseudogap at the Fermi level [10–12]. Graf *et al.* [13] reported that Fe_2VAl is located at a nonmagnetic node on the Slater-Pauling curve of the spontaneous ferromagnetic moment m in multiples of Bohr magnetons μ_B , where m scales with the total number of valence electrons following the rule $m = Z - 24$, and Z is the number of valence electrons (see also [14]). However, the weak ferromagnetism of this compound can be activated by atomic defects of AS Fe, as documented by DFT calculations. Numerous previous reports [15–17] have documented that antisite defects associated with Fe and V sites create local heterogeneous electronic states in Fe_2VAl , quite different compared to the nonmagnetic and semimetallic state of a defect free sample. The *ab initio* band structure calculation gives a magnetic AS Fe at the V site, when it is surrounded by four Fe atoms occupying Fe Wyckoff positions. There are also other AS defects that can be formed in $\text{Fe}_2\text{VAl}_{1+\delta}$, we therefore expect a variety of emergent phenomena resulting from the disorder introduced as a result of antisite defects and off-stoichiometry. We document experimentally complex magnetic behavior for $\text{Fe}_2\text{VAl}_{1.35}$. Our attention will be focused on the low temperature enhancement in magnetic susceptibility with singularity $\chi \sim T^{-1+\lambda}$, as well

as magnetization $M \sim B^\lambda$ behavior, both are reminiscent of a Griffiths-McCoy singularity [18, 19].

The experimental data for $\text{Fe}_2\text{VAl}_{1.35}$ are discussed with respect to those of nonmagnetic and metallic Ni_2VAl [77, 79, 80], which recently has been reported as a candidate for superconductivity [23]. Our investigations have not supported Ni_2VAl as a superconductor. It has been shown, however, that disorder of AS-type generates a weak magnetic moment located on Ni at AS position. In consequence of the AS disorder, the resistivity has a $\rho \sim -\ln T$ behavior in the temperatures $T < 10$ K, which characterizes Ni_2VAl as a diluted Kondo system. Moreover, accompanying spin fluctuations are detected with characteristic maximum in $\chi(T)$ at about 120 K, which seems to be interesting (see Sec. III.A and D).

II. EXPERIMENTAL AND COMPUTATIONAL DETAILS

A. Measurements

Polycrystalline samples of $\text{Fe}_2\text{VAl}_{1.35}$, V_2FeAl and $\text{Ni}_2\text{VAl}_{1.08}$ were prepared by the arc melting technique and subsequent annealing at 800°C for 2 weeks. The products were examined by x-ray diffraction (XRD) analysis (PANalytical Empyrean diffractometer equipped with a $\text{Cu } K\alpha_{1,2}$ source) and found to have a face-centered cubic $L2_1$ crystal structure (space group $Fm\bar{3}m$). The XRD patterns were analyzed with the Rietveld refinement method using the Fullprof Suite set of programs [24]. Figure 1 shows an XRD pattern for $\text{Fe}_2\text{VAl}_{1.35}$ (a) and $\text{Ni}_2\text{VAl}_{1.08}$ (b) with Rietveld refinements. The results presented in Table I were obtained for each sample with the weighted-profile R factors [25] $R_{wp} < 1.8\%$ and $R_{Bragg} < 0.9\%$. Stoichiometry and ho-

TABLE I. Lattice parameters a and stoichiometry.

compound	a (Å)	composition (at%)
$\text{Fe}_2\text{VAl}_{1.35}$	5.7659(8)	45.86 : 23.02 : 31.13
$\text{Ni}_2\text{VAl}_{1.08}$	5.7996(9)	49.48 : 24.25 : 26.27
V_2FeAl	5.9469(5)	49.55 : 25.11 : 25.34

mogeneity were checked using an electron energy dispersive spectroscopy (EDS) technique. The atomic percentage of the specific element content in Fe_2VAl , Ni_2VAl , and V_2FeAl is listed in Table I. For Ni_2VAl , and V_2FeAl it deviates from the nominal composition 2 : 1 : 1 at an acceptable level, while $\text{Fe}_2\text{VAl}_{1.35}$ was identified as off-stoichiometric with excess of Al and with a homogeneous distribution of atoms.

The ac magnetic susceptibility was measured in the temperature range 2-300 K with an ac field of 2 Oe and frequency from 100 Hz to 4 kHz using a Quantum Design PPMS platform. The dc magnetic measurements were carried out in the temperature interval

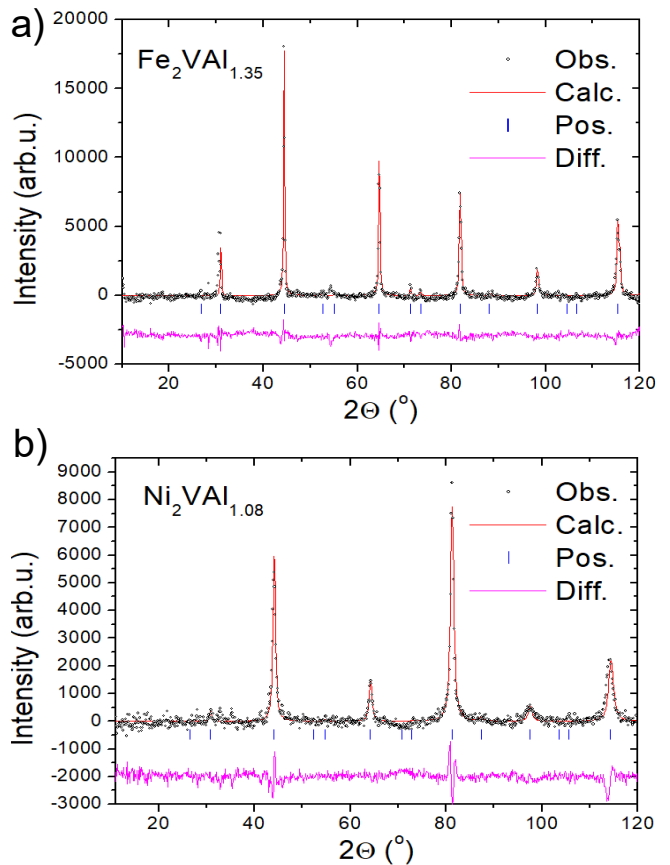


FIG. 1. Plot of Rietveld refinement for $\text{Fe}_2\text{VAl}_{1.35}$ (a) and $\text{Ni}_2\text{VAl}_{1.08}$ (b). Black dots - observed pattern, red line - calculated, blue ticks - Bragg peaks positions, magenta line - the difference. The $\text{Ni}_2\text{VAl}_{1.08}$ alloy is extremely hard, so the stresses when preparing the sample for XRD analysis cause a greater spread of background intensities in the XRD diffraction pattern.

1.7 – 400 K and magnetic fields up to 7 T employing a Quantum Design superconducting quantum interference device (SQUID) magnetometer. Time-dependent remnant magnetization and high-temperature dc magnetic susceptibility ($300 < T < 800$ K) were measured using the PPMS platform equipped with a vibrating sample magnetometer (VSM) option. Electrical resistivity and heat capacity measurements were performed in the temperature range 1.8 – 300 K and in external magnetic fields up to 9 T using the same PPMS platform.

The x-ray photoelectron spectroscopy (XPS) spectra were obtained at room temperature with monochromatized $\text{Al } K\alpha$ radiation using a PHI 5700/600 ESCA spectrometer. To obtain good quality XPS spectra, the samples were cleaved and measured in the vacuum of 6×10^{-10} Torr.

B. Computational methods

The electronic and magnetic properties of Fe_2VAl and Ni_2VAl , as well as the off-stoichiometry components, were theoretically studied using the *ab initio*, DFT-based full potential linearized augmented plane waves (FP-LAPW) method complemented with local orbitals (LO) [26]. The calculations were performed using the WIEN2k (ver. 19.1) package [27]. The atomic core states were treated within the fully relativistic DFT approach. For the local orbitals and valence states, (assumed as follows: V - $[3s^23p^6]_{\text{LO}}\{3d^34s^2\}_{\text{VB}}$; Fe - $[3s^23p^6]_{\text{LO}}\{3d^64s^2\}_{\text{VB}}$; Ni - $[3s^23p^6]_{\text{LO}}\{3d^84s^2\}_{\text{VB}}$ and Al - $[2s^22p^6]_{\text{LO}}\{3s^23p^1\}_{\text{VB}}$) the scalar-relativistic Kohn-Sham formalism was applied with spin-orbit coupling (SOC) accounted for through the second variational method [26]. The generalized gradient approximation (GGA) for the exchange-correlation (XC) energy functional was applied in the form derived for solids by Perdew *et al.* (PBEsol) [28]. For the correlated d states, the XC potential was corrected by on-site Hubbard-like interaction U following the Anisimov *et al.* approach [29, 30]. In the calculations presented, we assumed the effective Hubbard parameter $U_{\text{eff}} (= U - J)$ for d -states of Fe, Ni, and V we assumed equal to 3 eV.

For simulations of off-stoichiometric systems with antisite atoms, we employed the supercell spanned by doubled primitive vectors of the underlying L2_1 primitive cell, comprising eight formula units of Fe_2VAl (Ni_2VAl), based on which the superstructures were prepared with Al, Fe, Ni, and V atoms located at antisite positions. The calculations were performed for a basic Fe_2VAl and Ni_2VAl structures and superstructures with compositions: $\text{Fe}_{16}(\text{V}_7\text{Fe}_1)\text{Al}_8$, $\text{Fe}_{16}(\text{V}_7\text{Al}_1)\text{Al}_8$, $\text{Fe}_{16}(\text{V}_5\text{Al}_3)\text{Al}_8$, $(\text{Fe}_{15}\text{Al}_1)\text{V}_8\text{Al}_8$, $(\text{Fe}_{13}\text{Al}_3)\text{V}_8\text{Al}_8$, and $\text{Ni}_{16}(\text{V}_7\text{Ni}_1)\text{Al}_8$. Structural analysis revealed that the antisite atoms in the vanadium sublattice do not change the space group $\text{Fm}\bar{3}\text{m}$ (no. 225) of the original Heusler structure, while those located in the Fe sublattice reduce the space group of the corresponding superstructure to the F43m (no. 216). Nevertheless, in all cases, the disorder caused by AS atoms, connected to the anisotropy introduced by the spin-orbit coupling, split the Wyckoff positions of the Heusler structure into several subgroups (see Table III).

In the presented approach, the parameters decisive for the accuracy of the calculations employing the WIEN2k code, the number of \vec{k} vectors in the Brillouin zone (BZ), and the plane wave cut-off energy (K_{max}) were tested against the total energy convergence. A satisfactory energy precision of few meV for the base Fe_2VAl and Ni_2VAl was reached with $12 \times 12 \times 12$ k-mesh (163 \vec{k} vectors in irreducible BZ) and $K_{\text{max}} = 9/R_{\text{MT}}$. The radii of the muffin-tin spheres R_{MT} of 0.1058 nm were assumed as common for all atomic species. These settings were also adopted in the calculations for superstructures.

III. MAGNETIC AND TRANSPORT PROPERTIES IN DISORDERED $\text{Fe}_2\text{VAl}_{1.35}$ IN REFERENCE TO SPIN-FLUCTUATOR Ni_2VAl , EXPERIMENTAL DETAILS AND DISCUSSION

A. Magnetic properties

The magnetic and transport properties of Heusler alloys are highly dependent on stoichiometry, as well as the level of atomic disorder. Here we present the magnetic properties of $\text{Fe}_2\text{VAl}_{1+\delta}$ with excess of Al ($\delta \sim 0.35$) with respect to $\text{Ni}_2\text{VAl}_{1+\delta}$ ($\delta \sim 0.08$), we also discuss the impact of antisite defects on the localization of $3d$ electronic states of Fe and Ni in both alloys. A detailed analysis of the complex magnetic behaviors documented for $\text{Fe}_2\text{VAl}_{1+\delta}$ is also based on other thermodynamic and electron transport studies (in Sec. III.B-D), as well as *ab initio* electronic structure calculations, presented in Sec. IV.

Shown in Fig. 2 are the dc magnetic susceptibility χ data plotted as χ and $1/\chi$ vs. T between 1.7 and 700 K for $\text{Fe}_2\text{VAl}_{1.35}$. The susceptibilities of $\text{Ni}_2\text{VAl}_{1.08}$ and V_2FeAl measured in the temperature region $T < 300$ K are also displayed for comparison. The $\chi^{-1}(T)$ follows a

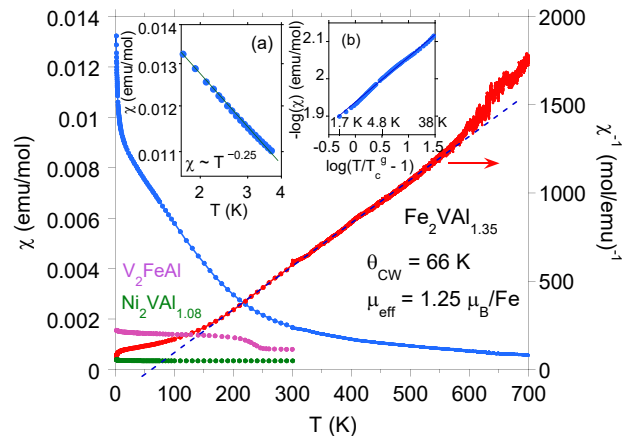


FIG. 2. Temperature dependence of dc χ (blue points) and $1/\chi$ (red points) at 1000 G for $\text{Fe}_2\text{VAl}_{1.35}$. For comparison, the dc susceptibility $\chi(T)$ at 1000 G are shown for V_2FeAl (pink points) and for $\text{Ni}_2\text{VAl}_{1.08}$ (green points). Inset (a) shows the divergent behavior of χ for $T < 4$ K, inset (b) presents $1/\chi$ vs. reduced T , $(T/T_c^g - 1)$ in the log-log scale. We attribute the change in the susceptibility of $\text{Fe}_2\text{VAl}_{1.35}$ that occurs at ~ 580 K to a diffusion process that results in a more highly ordered sample above this temperature.

Curie law above ~ 600 K with the effective magnetic moment $\mu_{\text{eff}} = 1.26 \mu_B$ per one Fe atom in the formula unit. A very crude analysis predicts that statistically only one iron atom contributes to the value of μ_{eff} per unit cell of $\text{Fe}_2\text{VAl}_{1+\delta}$, assuming that only Fe ions contribute to the effective magnetic moment and $\mu_{\text{eff}}(\text{Fe}^{2+}) = 5.4 \mu_B$. Magnetization as well as the specific heat data suggest one order of magnitude smaller number of magnetic Fe defects in this system (will be discussed). DFT calcu-

lations confirm that this is an Fe ion in the antisite position, while the remaining Fe atoms in the surrounding of the AS defect are *non-magnetic* (will be discussed in Sec. IV). A Curie-Weiss (CW) law is obeyed in the range of $200 < T < 580$ K, indicating a peculiar magnetic state with random magnetic interactions below ~ 200 K and signaling the onset of weak ferromagnetism. The best fit to $\chi \sim (T - \theta_{CW})^{-1}$ gives the CW temperature $\theta_{CW} = 66$ K and $\mu_{\text{eff}} = 1.25 \mu_B$ per Fe atom, i.e., almost four times smaller value of μ_{eff} than that predicted for Fe^{2+} . The magnetic susceptibility anomaly below 200 K has been found to arise from a distribution of magnetic defects in the sample (cf. Refs. [17]). Similar anomalous behaviors in χ appear to be characteristic of the family of Heusler alloys containing the magnetic transition metal M , regardless of the stoichiometry of the system (cf. $\chi(T)$ data for V_2FeAl in Fig. 2), while it is not present in *almost paramagnetic* $\text{Ni}_2\text{VAl}_{1.08}$. As an example, a well ordered V_2FeAl is expected to be a Pauli paramagnet [31, 32], while a weak magnetization below ~ 230 K can be induced in this material by wrong-site iron atoms as a result of incomplete structural ordering, as shown in Fig. 2. Our investigations suggest a similarity of this weakly magnetic state with short-range magnetic correlations with the behavior of the Griffiths phase (GP) scenario [18]. The distinct similarities to the Griffiths phase have already been suggested earlier for the off-stoichiometric Fe_2VAl [9], as well as for the $(\text{FeNi})\text{TiSn}$ alloy [33] and disordered Fe_2VAl [34] due to the presence of AS defects.

The Griffiths phase consists of magnetic clusters in a paramagnetic phase much above T_C and forms as a result of the competition between the Kondo effect and the Ruderman-Kittel-Kasuya-Yosida (RKKY) interaction in the presence of disorder [18]. Namely, in the temperature region $T_C^g < T < T_G$, where T_G is a Griffiths temperature, the system is considered to exist in the GP that exhibits neither pure paramagnetic behavior nor long-range ferromagnetic (FM) order. In this framework, the Griffiths phase is a peculiar state that is predicted to occur in randomly diluted Ising FM systems [35, 36], in which magnetization fails to become an analytic function of the magnetic field over a temperature range $T_C^g < T < T_G$. Usually, Griffiths singularity is signed by a nonlinear variation of the inverse magnetic susceptibility in the paramagnetic phase [37], namely $\chi^{-1} \propto (T - T_C^g)^{-(1-\lambda)}$ ($0 < \lambda < 1$) [38, 39], where T_C^g is the critical temperature of random ferromagnetism of the sample where susceptibility tends to diverge. According to the χ -data shown in Fig. 2, the deviation from the CW law is evidenced for $T < 200$ K, while below $T = 4$ K the dc susceptibility exhibits a power-law behavior, $\chi \sim T^{-n}$, with exponent $n = 1 - \lambda = 0.25$ [38]. Moreover, for $1.7 < T < 40$ K χ can be well characterized by expression $\chi(T) \sim (T - T_C^g)^{-(1-\lambda)}$ with the fitting parameters $T_C^g = 1.3$ K and $\lambda = 0.7$.

According to the GF scenario, χ shown in Fig. 2 deviates from the CW law below $T \equiv T_G = 200$ K, while

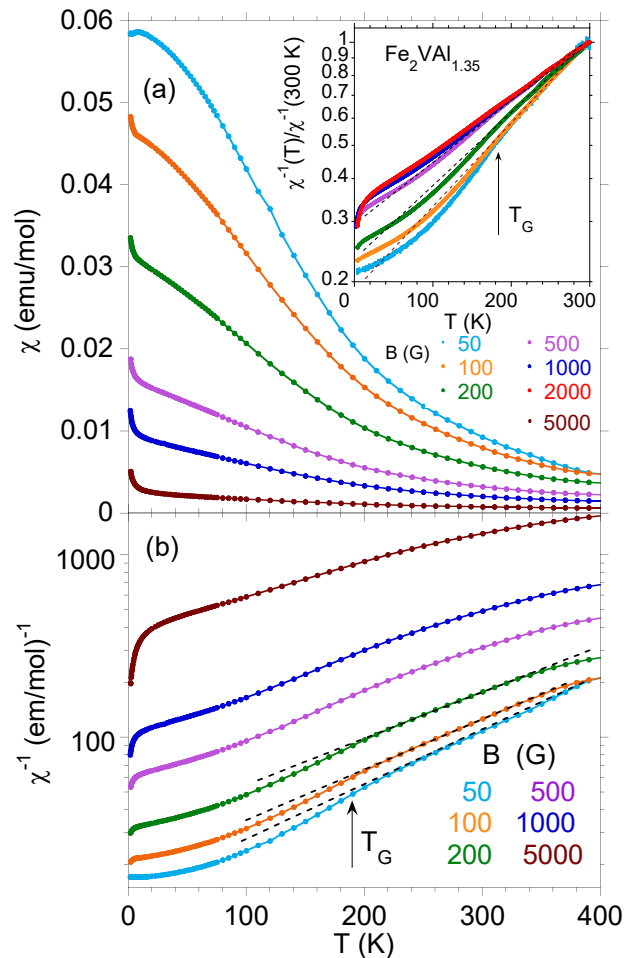


FIG. 3. (a) Susceptibility and (b) inverse susceptibility (in log scale) vs temperature data from QD SQUID magnetometer, measured for $\text{Fe}_2\text{VAl}_{1.35}$ in different values of applied fields. The inset shows similar data of $\chi(T)^{-1}$ normalized to $1/\chi$ at 300 K (in log scale) obtained from a commercial QD PPMS-VSM platform. The dashed lines approximate the CW behavior to low temperatures to show the downward effect in χ^{-1} below temperature $T_G \sim 200$ K.

for $T < 4$ K susceptibility exhibits a power-law behavior, $\chi \sim T^{-n}$, with exponent $n = 1 - \lambda = 0.25$ [38]. Moreover, for $1.7 < T < 40$ K χ can be well characterized by expression $\chi(T) \sim (T - T_C^g)^{-(1-\lambda)}$ with the fitting parameters $T_C^g = 1.3$ K and $\lambda = 0.7$. Fig. 3 shows the $\chi(T)$ dc data measured at various magnetic fields $50 < B < 5000$ G. In the field of 50 G χ exhibits a maximum at ~ 9 K indicative of a magnetic glassy behavior, while χ measured at larger fields shows divergent behavior at the lowest temperatures. The inset to Fig. 3 presents the inverse susceptibility divided by the value of χ^{-1} at 300 K in different fields as a function of T from the VSM experiment, to show more details. For $T > 200$ K χ^{-1} varies linearly with T , following the CW behavior. However, with the decrease in T , a clear downturn in χ^{-1} is observed at $T \approx 200$ K (much above T_C^g) for the measurements performed in dc fields $B \leq 500$ G, indicating

non-analytic behavior of M arising from the Griffiths singularity. The softening of the *downward* behavior in χ^{-1} and the progressive increase of χ^{-1} in the field (cf. Fig. 3) are characteristic properties of the GP state (cf. [39]), both allowed to distinguish the Griffiths singularity from smeared phase transition between the paramagnetic and ferromagnetic states.

We also comment on the field-induced divergence of the value of χ , shown for $\text{Fe}_2\text{VAL}_{1.35}$ in Fig. 3. This field-dependent $\chi(T)$ plots may result from a trace amount of magnetic Fe impurities, can be caused by spin fluctuations quenched by the field (cf. [40, 41]), and/or may be caused by the various size of clusters field-dependent. For the first scenario, the appearance of Fe impurities should cause an increase in χ with an increasing field; this is not a case. The effect of spin fluctuations on the value of χ seems to be possible for $\text{Fe}_2\text{VAL}_{1.35}$ since similar field-induced $\chi(T)$ behavior has also been observed for spin-fluctuator Ni_2VAL . Note that spin fluctuation gives a dominant effect around T_C , but is also important much above T_C , since the energy scale of spin fluctuations is usually two orders of magnitude larger than T_C for itinerant electron ferromagnets [42, 43]. The magnetic properties shown in Fig. 3 are more likely the result of contributions from both fluctuating moments and cluster size effects, as has been reported for a variety of nanoparticles (e.g., Refs. [44–46]).

The ac magnetic susceptibility was measured at various frequencies in order to confirm the hypothesis of spin/cluster-glass state in $\text{Fe}_2\text{VAL}_{1.35}$. Shown in Fig. 4 are the real (χ') and imaginary (χ'') components of the magnetic ac susceptibility data. χ' [in panel (b)] and χ'' [in panel (c)] exhibit a broad maxima at ~ 15 K with amplitudes and positions depending on the frequency ν of the applied magnetic field. The maximum of χ' can be attributed to a spin-glass-like transition, which is commonly used to determine the spin freezing temperature T_f . The frequency dependence of T_f follows the empirical Vogel-Fulcher relation that is described as $\nu = \nu_0 \exp[-E_a/k_B(T_f - T_0)]$, where ν_0 , T_0 , and E_a are fitting parameters [47]. Taking into account the microscopic single spin flipping frequency $\nu_0 \sim 10^{13}$ Hz for spin-glass materials we obtained $E_a = 290$ K and $T_0 = 1.7$ K, fitting this expression to the linear change of T_f versus $1/\ln(\nu_0/\nu)$. The parameter T_0 does not have a precise physical meaning; it is proposed to be related to the true critical temperature when $T_f > T_0$ is only a dynamic manifestation of the magnetic transition from paramagnetic to SG phase, cf. Ref. [47]. The frequency shifts of the χ' maxima yield ratio $\delta T_f = \Delta T_f/T_f \Delta \log_{10} \nu \approx 0.02$, which is one order of magnitude higher than expected for canonical metallic spin-glass materials ($\sim 10^{-3}$), but fits well with the range that is reported for cluster-glasses [47]. Fig. 6 shows quite different behavior in $\chi_{ac}(T)$ for $\text{Ni}_2\text{VAL}_{1.08}$, namely, a broad maximum in χ' is observed at about 100 K, which is indicative of the spin fluctuations.

We have studied the isothermal magnetic relaxation

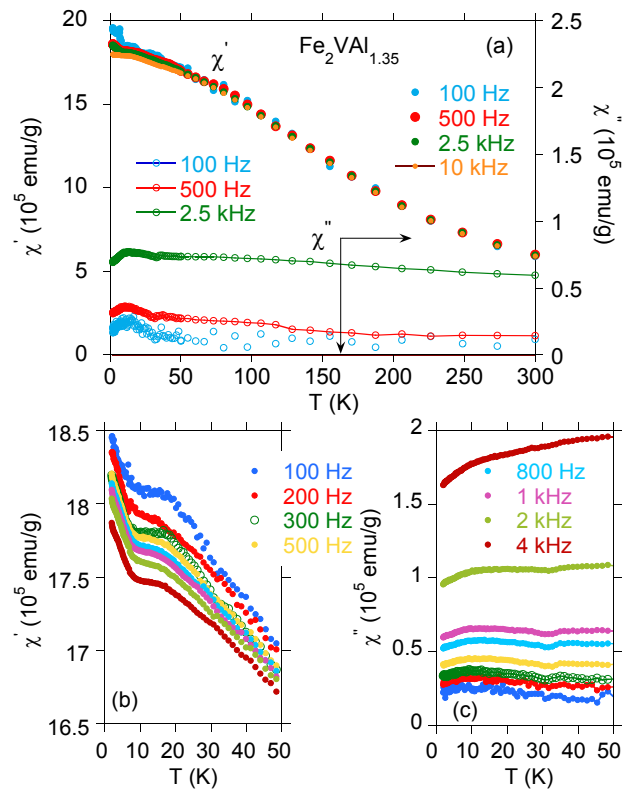


FIG. 4. Temperature dependence of the real and imaginary part of the ac magnetic susceptibility χ_{ac} for $\text{Fe}_2\text{VAL}_{1.35}$ measured for various frequencies of the applied magnetic field; the amplitude of the magnetic field was 2 G. Panels (b) and (c) show details over a limited temperature range for $T < 50$ K. Panel (b) shows the obvious *step-like* changes in χ' at about 20 K, 30 K, and 40 K, which are magnified for clarity in Fig. 5.

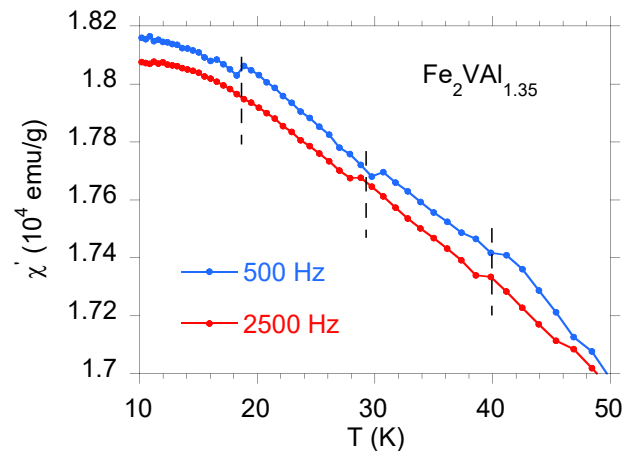


FIG. 5. Magnetic susceptibility χ' as a function of temperature; drops in M' during stops at 19, 30 and 41 K are magnified for clarity (cf. Fig. 4) and will be discussed in Sec. III.B.

phenomenon in $\text{Fe}_2\text{VAL}_{1.35}$ and $\text{Ni}_2\text{VAL}_{1.08}$ as a final test of glassy state formation in these alloys. The samples

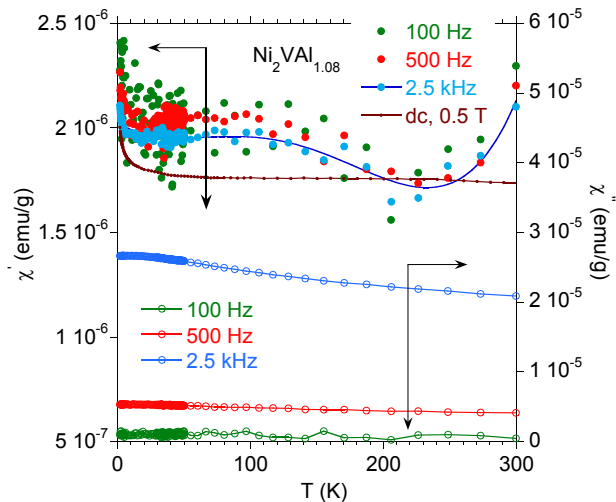


FIG. 6. Temperature dependence of the real and imaginary part of the ac magnetic susceptibility χ_{ac} for $\text{Ni}_2\text{VA}_{1.05}$ measured for various frequencies of the applied magnetic field; the amplitude of the magnetic field was 2 G. Comparison with dc magnetic susceptibility measured for $\text{Ni}_2\text{VA}_{1.05}$ in the field 5000 G.

were first zero field cooled from 300 K down to 8 K with a constant cooling rate and kept at a target temperature for a waiting time $t_w = 300$ s in the field of 5000 G. Then the field was switched off. Figure 7 displays the time evolution of magnetization M measured in zero-field-cooled (ZFC) mode at temperature 8 K for an applied field of 0.04 G. Various functional forms have been proposed to describe magnetization as a function of observation time [47]. The time dependence of M shown in Fig. 7 for $\text{Fe}_2\text{VA}_{1.35}$ is well approximated by the expression for magnetic viscosity $M(t) = M(0) + S \ln(1 + t/t_0)$, where $M(0)$ is the magnetization at $t = 0$, $t_0 = 375$ s is the reference time, and $S = 2.3 \times 10^{-4}$ emu/g is the magnetic viscosity. The reference time t_0 is typically orders of magnitude larger than the observed microscopic spin flip τ_0 . The estimated values of S are comparable to the results reported for other glassy systems. The magnitude of $M(t)$ strongly depends on t_w before switching on the field [47]. However, this behavior is out of the scope of this research. Alternatively, $M(t)$ can be well approximated by an expression $M(t) = M_0 + M_r \exp[-(t/\tau_r)^{1-n}]$, where magnetization $M(0) = 0.0092$ emu/g could be interpreted as an intrinsic weakly *ferromagnetic* component that appears below ~ 200 K in effect of sample disorder (cf. Fig. 2), while $M_r = 0.0031$ emu/g could be related to a glassy component that mainly contributes to the relaxation effects observed. Within the disordered scenario, the magnetic clusters of Fe are distributed in the weakly *magnetic* background. In this approximation, the time constant $\tau_r = 1.8 \times 10^5$ s and the parameter $n = 0.35$ [48] are related to the relaxation rate of the spin-glass-like phase [49]. Figure 7 compares a similar isothermal remnant magnetization (IRM) as a function of time, measured for $\text{Ni}_2\text{VA}_{1.08}$ at 8 K under the

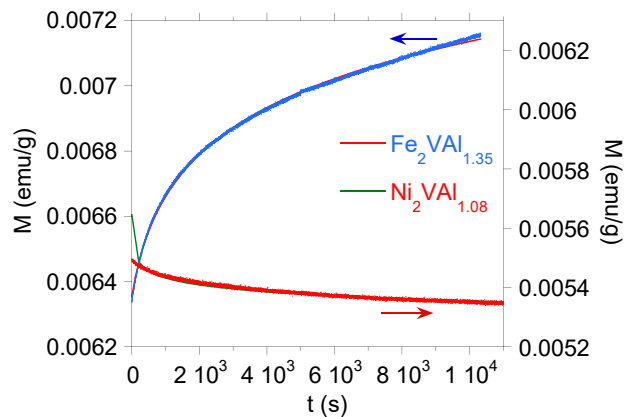


FIG. 7. Time dependent remnant magnetization behavior for $\text{Fe}_2\text{VA}_{1.35}$ (blue points) and $\text{Ni}_2\text{VA}_{1.08}$ (red points). The red solid line represents a fit to equation $M(t) = M(0) + S \ln(1 + t/t_0)$, the green solid line represents the best fit to equation $M(t) = M(0)t^{-\alpha}$.

same conditions. The observed time dependence of IRM is weakly t -dependent and can be fitted by the power-law decay, $M(t) = M(0)t^{-\alpha}$ with the fitting parameter $\alpha = 6.2 \times 10^{-3}$, however, only for $t > 200$ s. Below this time limit, the $M(t)$ data do not follow the $M(0)t^{-\alpha}$ behavior. The $M(t)$ dependence shown for $\text{Ni}_2\text{VA}_{1.08}$ in Fig. 7 signals the presence of diluted and disordered magnetic moments of AS Ni defects (will be discussed) which, however, do not form an ordered glassy state.

To further probe the nature of the magnetic ground state in $\text{Fe}_2\text{VA}_{1.35}$ and $\text{Ni}_2\text{VA}_{1.08}$ Heusler alloys, the isothermal magnetization M was measured as a function of magnetic field, as shown in Fig. 8. The $M(B)$ isotherms of $\text{Fe}_2\text{VA}_{1.35}$ do not exhibit any hysteresis loop, however, are also not characteristic of paramagnets. The $M(B)$ characteristics cannot be approximated by the Langevin function $L(\xi) = \coth(\xi) - 1/\xi$ ($\xi = \mu B/k_B T$ and μ is the total magnetic moment), as shown in panel (a). Moreover, M is not a universal function of B/T as displayed in the inset to Fig. 8(a). This scaling behavior is characteristic of the superparamagnetic state, which is not the case. Whereas, magnetization as a function of the field up to 7 T follows the predicted Griffiths phase behavior $M \sim B^\lambda$ [50], as shown in Fig. 8(a). Within the Griffiths phase scenario the $M \sim B^\lambda$ well approximates the experimental data and gives $\lambda = 0.76$ for the $M(B)$ data at $T = 10$ K. The fitting procedure of M at $T = 1.7$ K gives $\lambda \sim 0.45$ smaller than expected, the reason is due to the increase of magnetic correlations for $T \rightarrow T_C^g$ that lead to a glassy state and dominate the Griffiths phase state. Figure 8(b) displays the paramagnetic M vs. B behavior for $\text{Ni}_2\text{VA}_{1.08}$ at 1.7 K, well approximated by the Langevin function $L(\xi)$.

Finally, we present some notes on the magnetic ground state in the disordered Fe alloy. While the parent compound Fe_2VA has a *nonmagnetic* ground state, its disordered analogues determined by the presence of vacan-

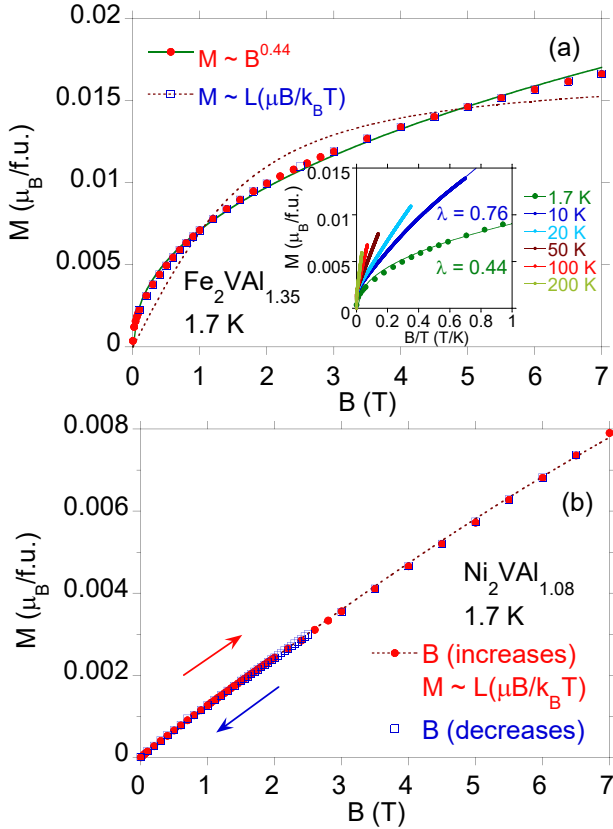


FIG. 8. Isothermal magnetization as a function of applied magnetic field of $\text{Fe}_2\text{VA}_{1.35}$ (a) and $\text{Ni}_2\text{VA}_{1.08}$ (b) for 1.7 K. The red dotted line is a fit of the Langevin function L to the magnetization data. In panel (a) the green line shows the approximation of the expression $M = M(0) + mB^\lambda$ to the experimental data. The inset displays M vs B/T ; in this plot the M isotherms are approximated by the $M \sim B^\lambda$ expression for $T = 1.7$ K and 10 K, respectively.

cies at various crystallographic sites, off-stoichiometry, and/or doping are very close to ferromagnetic ordering, as has been demonstrated by many studies (cf. Ref. [41] and references therein). The divergence in the $\chi(T)$ data shown in Fig. 2 suggests this possibility at the limit of $T \rightarrow 0$.

B. Memory effect in $\text{Fe}_2\text{VA}_{1.35}$

The non-zero value of $M(0)$ in Fig. 7 indicates the coexistence of weakly magnetic and glassy magnetic components in the relaxation process. It can be assumed that the small clusters of Fe are separated in the weakly magnetic phase. The phase separation scenario would be favorable to explain the existence of out-of-equilibrium features shown in $\chi'(T)$ data in Figs. 4 and 5, as competition between coexisting phases, leading to the appearance of locally metastable states observed in ac susceptibility, as memory effect in the cooling cycle. In our ac magnetization measurements, a field with an amplitude

of 2 G was applied during cooling. An analogous behavior was observed for Fe-doped phase separated manganite $\text{La}_{0.5}\text{Ca}_{0.5}\text{MnO}_3$ [51] and for $\text{Dy}_{0.5}\text{Sr}_{0.5}\text{MnO}_3$ [52].

C. Specific heat

Fig. 9 compares the temperature dependence of the specific heat for $\text{Fe}_2\text{VA}_{1.35}$ and of $\text{Ni}_2\text{VA}_{1.08}$, measured in a zero magnetic field. For both alloys, the value of C per one atom reaches the value of $3R$ in accordance with the Dulong-Petit law (R is the gas constant). The $C(T)$ data are well approximated by the Debye-Einstein (DE) model [53]:

$$C(T) = \gamma_0 T + 9NR(1-d) \left(\frac{T}{\Theta_D}\right)^3 \int_0^{\Theta_D/T} \frac{x^4 e^x}{(e^x - 1)^2} dx + 3nRd \left(\frac{\theta_E}{T}\right)^2 \frac{e^{\theta_E/T}}{(e^{\theta_E/T} - 1)^2}, \quad (1)$$

where the first term is the electron specific heat $C_{el}(T) = \gamma_0 T$, and the two others account for the lattice contributions (θ_D and θ_E are the Debye and Einstein temperatures, respectively, n is the number of atoms per formula unit, and d stands for the number of optical phonon modes).

The solid lines show temperature variation of the calculated $C(T)$ with the fitting parameters $\gamma_0 = 33$ mJ/molK², $\theta_D = 638$ K, $\theta_E = 297$ K, and $d = 0.51$ for $\text{Fe}_2\text{VA}_{1.35}$, and respective set of the fitting parameters for $\text{Ni}_2\text{VA}_{1.08}$ ($\gamma_0 = 11$ mJ/molK², $\theta_D = 492$ K, $\theta_E = 148$ K, and $d = 0.69$). Equation (1) does not take into account the magnetic contributions from the spin glass state, therefore, at the temperatures $T < 20$ K the fitting is not satisfactory for $\text{Fe}_2\text{VA}_{1.35}$, which is the reason for the overestimated value of γ_0 .

The γ_0 and β_0 derived from the linear sections (for $T > 6$ K) of C/T vs T^2 dependence are 5.5 mJ/K² mol and 4.6×10^{-5} J/K⁴ mol, respectively, indicating the pseudogap in the bands of $\text{Fe}_2\text{VA}_{1.35}$ at the Fermi level. The γ_0 and β_0 determined similarly for $\text{Ni}_2\text{VA}_{1.08}$ in the temperature range $T < 15$ K are respectively, 13.5 mJ/K² mol and 2.6 J/K⁴ mol. Moreover, these fitting parameters obtained from the approximation of Eq. (1) to $C(T)$ as well those from linear dependence of C/T vs. T^2 are similar. For $N = 4$ atoms in formula unit, $\beta = N(12/5)\pi^4 R \theta_D^{-3}$ gives the Debye temperature, $\theta_D \sim 567$ K for $\text{Fe}_2\text{VA}_{1.35}$ and $\theta_D \sim 304$ K for $\text{Ni}_2\text{VA}_{1.08}$, respectively. In both cases, the determined temperatures θ_D are close to those obtained by fitting the DE function [Eq. (1)] to the $C(T)$ data.

Inset (b) displays the low-temperature specific heat C divided by temperature, $C(T)/T$, at various magnetic fields for $\text{Fe}_2\text{VA}_{1.35}$. The upturn in C/T at $B \neq 0$ can be interpreted as a result of Schottky-like anomalies due to magnetic defects [54, 55]. Assuming that the specific heat is a sum, $C_{\text{magn}} + \gamma T + \beta T^3$, the C/T data at various magnetic fields are well approximated to expression

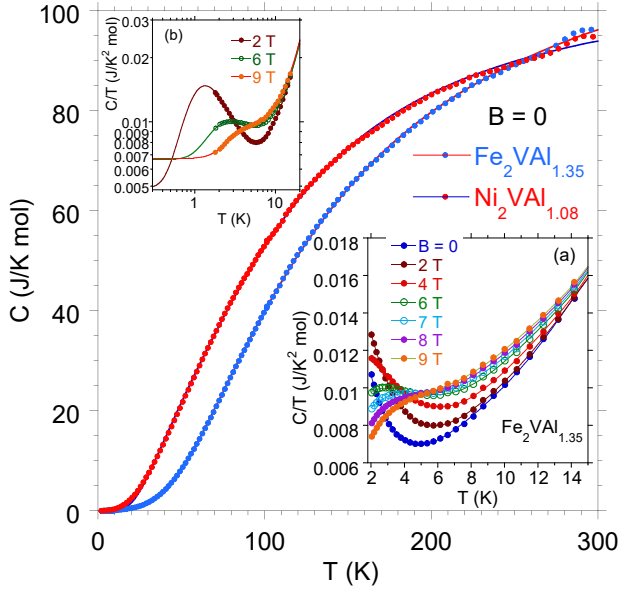


FIG. 9. Specific heat for $\text{Fe}_2\text{VAI}_{1.35}$ (blue points) and $\text{Ni}_2\text{VAI}_{1.08}$ (red points) measured in a wide temperature range and a fit of Eq. (1) to the experimental data. In panel (a), the temperature dependence of C/T in various magnetic fields. The continuous curves are the fits of a two-level Schottky-like function C_{Sch} , lattice βT^3 , and electronic γT contributions to the C/T data (cf. Table II). The inset (b) shows in detail the approximation of the two-level Schottky function to the experimental data C/T for Fe in the field of 2, 6, and 9 T.

$C/T = C_{\text{Sch}}/T + \gamma + \beta T^2$, where C_{Sch} is a two-level Schottky function

$$C_{\text{Sch}} = N_{Fe} k_B \left(\frac{\epsilon}{T} \right)^2 \frac{e^{\epsilon/T}}{(1 + e^{\epsilon/T})^2}, \quad (2)$$

with ϵ , γ , and β field dependent (cf. Table II). In the inset (b) to Fig. 9 the solid lines are the best fits of $C_{\text{Sch}}/T + \gamma + \beta T^2$ to the C/T experimental data of $\text{Fe}_2\text{VAI}_{1.35}$. A simple fit of the Schottky function to $C(T, B = 0)$ data gives $\sim 10 \times 10^{19} \text{ cm}^{-3}$ of Schottky centers N_{Fe} . Assuming that Fe_{AS} defects dominate in the sample, and taking $g = 1.93$ and $S = 3/2$ for the antisite defects, the saturation magnetization of $\text{Fe}_2\text{VAI}_{1.35}$ (cf. Fig. 8a) expressed by $M_S = N_{Fe} g \mu_B S$ gives comparable *magnetic impurity* concentration of $\sim 13 \times 10^{19} \text{ cm}^{-3}$ which, when calculated per unit cell, gives about 0.02 atom per cell in the antisite position. One also notes that the ϵ vs. B change is well approximated by expression $\epsilon(B) = \epsilon(0) + bB^n$ with exponent $n = 1.6$, moreover, in the constant field mode, each value of ϵ/k_B is obtained twice larger than the value of $T \equiv T_f$ at which $C_{B=\text{const}}(T)/T$ has the maximum.

Figure 10 shows the electronic specific-heat constant γ_0 and the coefficient of the T^3 term β for Fe and Ni samples as a function of the magnetic field. It is worth noting that the field dependencies either of γ_0 and β are for $\text{Ni}_2\text{VAI}_{1.08}$ typical for systems with spin fluctuations.

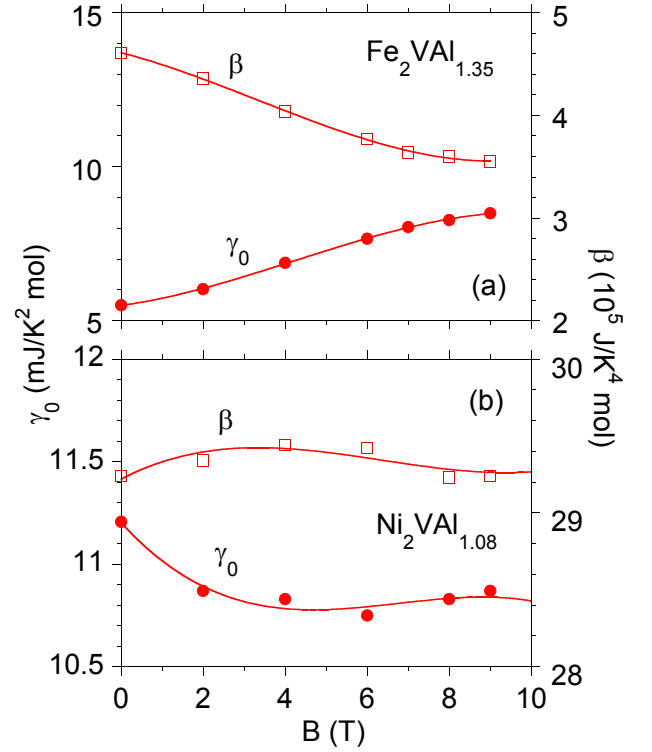


FIG. 10. Electronic specific heat coefficient γ_0 and coefficient β vs applied magnetic field B . γ_0 and β are obtained from the linear dependence of $C(T)/T = \gamma_0 + \beta T^3$ vs. T^2 for $\text{Fe}_2\text{VAI}_{1.35}$ and for $\text{Ni}_2\text{VAI}_{1.08}$ in the temperature region between ~ 5 K and 15 K.

Namely, the field-induced behavior of γ_0 and β shown in panel (b) as well as $\chi(T)$ shown in Fig. 6 are similar to those, observed for canonical spin fluctuator CeSn_3 , which was classified by Ikeda et al. [56] as a type 3 spin fluctuator.

$\text{Fe}_2\text{VAI}_{1.35}$ exhibits significantly different corresponding characteristics, as shown in panel (a). An increase in γ_0 shown in Fig. 10 we attribute to a strong reducing of the pseudogap at the Fermi level by increasing the field, which consequently gives an increase of γ . Our previous research of similar Heusler alloys (Fe_2TiSn [17], Fe_2VSn [57]) explicitly documented that the physical properties of these semiconductors, in particular resistivity, susceptibility, and specific heat are dominated by crystallographic disorder. The AS atomic disorder can generate the narrow d -electronic band located at the Fermi level, which is responsible for the unusual temperature dependencies (these materials can also be discussed as false Kondo insulators).

Figure 11 shows entropy S for $\text{Fe}_2\text{VAI}_{1.35}$ and $\text{Ni}_2\text{VAI}_{1.08}$ in the temperature region $T < 100$ K. Assuming that only conduction electrons, phonons and spin fluctuations contribute to S , then the entropy of

TABLE II. Specific heat $C(T)$ parametrization of $\text{Fe}_2\text{VAl}_{1.35}$ within temperatures $T < 15$ K. $C(T)$ is fitted to the two-level Schottky function supplemented with electron (γT) and phonon (βT^3) contributions. Comparison with electronic specific heat coefficients γ_0 and coefficients β_0 experimentally obtained from a least-squares fit of expression $C(T)/T = \gamma_0 + \beta_0 T^2$ to the experimental data in the temperature region between ~ 5 K and 15 K (cf. Fig. 10).

B (T)	ϵ (K)	$C = N_{Fe} k_B (\epsilon/T)^2 e^{\epsilon/T} / (1 + e^{\epsilon/T})^2 + \gamma T + \beta T^3$			$C = \gamma_0 T + \beta_0 T^3$	
		γ (mJ/K ² mol)	$\beta \times 10^5$ (J/K ⁴ mol)	γ_0 (mJ/K ² mol)	$\beta_0 \times 10^5$ (J/K ⁴ mol)	
0	2	4.7	5.0	5.5	4.6	
2	3.2	4.9	4.8	6.0	4.4	
4	4.7	5.7	4.5	6.9	4.0	
6	6.2	6.7	4.1	7.7	3.8	
7	7.5	7.0	4.8	8.0	3.6	
8	9.0	7.1	4.0	8.3	3.6	
9	10.8	6.8	4.2	8.5	3.5	

$\text{Ni}_2\text{VAl}_{1.08}$ can be well fitted by expression [58]:

$$S = \int_0^T \frac{dC}{T} = \int_0^T \frac{\gamma_0 T + \beta T^3 + \delta T^3 \ln(T/T^*)}{T} dT$$

$$= \gamma_0 T + \frac{\beta}{3} T^3 + \frac{\delta}{3} T^3 \ln \frac{T}{T^*} - \frac{\delta}{9} T^3, \quad (3)$$

where $T^* = 120$ K, $\gamma_0 = 13$ mJ/K² mol, $\beta = 1.5 \times 10^{-4}$ J/K² mol, and $\delta = -1.7 \times 10^{-4}$ J/K⁴ mol (cf. Fig. 11). The fit is very good for $T > 30$ K, but for lower temperatures this approximation deviates from the experimental data, even within 10% around 15–20 K. A possible reason for this divergence may be the Kondo effect due to scattering of conduction electrons on magnetic Ni impurities, which can give an additional contribution to S (in Sec. IV we will document in *ab initio* calculations that Ni at AS positions has a localized magnetic moment). Figure 12 presents low-temperature C/T vs. T^2 data at various fields for $\text{Ni}_2\text{VAl}_{1.08}$, with an obvious and field-dependent upturn in C/T for $T^2 < 40$ K. This behavior is not typical of spin fluctuators for which the quenching of the magnetic contribution to the heat capacity by the magnetic field is usually detected. The possible explanation for the low-temperature heat capacity enhancement shown in Fig. 12 can be the formation of a Kondo resonance. Indeed, the heat capacity C/T measured in varying magnetic fields shows typical behavior of diluted Kondo systems [59, 60], and well correlates with the low- T resistivity data (see Sec. III.C).

Expression (3), however, does not fit well the S data of $\text{Fe}_2\text{VAl}_{1.35}$. In this case, the entropy shows a kink at $T \sim 3$ K due to freezing of the glassy phase (see the inset to Fig. 11), and can be well approximated by expression $S(T) \sim \gamma_0 T + \beta T^3 + sT^n$ with exponent $n = 3/2$ for $T < 3$ K and $n = -2$ for $T > 3$ K [61], respectively, as shown in Fig. 11 (for both cases, $\gamma_0 = 5.5$ mJ/K⁴ mol, $\beta = 1.9 \times 10^{-4}$ mJ/K⁴ mol).

D. Electron transport properties

Previous reports have indicated that even a small deviation in the stoichiometry of Fe_2VAl has a significant impact on its electron transport properties [15]. Similarly, the thermal heat treatment of this alloy has a decisive impact on its electric and thermal transport [62]. So far, electron transport investigations were focused on the Fe_2VAl alloys with a deficiency of both Fe, V and Al, mainly in terms of enhancing the thermoelectric properties. The aim of the current research was to demonstrate to what extent an excess of Al can change the thermoelectric properties of Fe_2VAl . However, our research did not confirm the expectations of significant strengthening of the thermoelectric properties of this alloy. The results obtained for $\text{Fe}_2\text{VAl}_{1+\delta}$ were compared with electron transport measurements for Ni_2VAl . Figure 13 compares the thermal conductivity κ , Seebeck coefficient S , and figure of merit ZT of $\text{Fe}_2\text{VAl}_{1.35}$ and $\text{Ni}_2\text{VAl}_{1.08}$. Panel

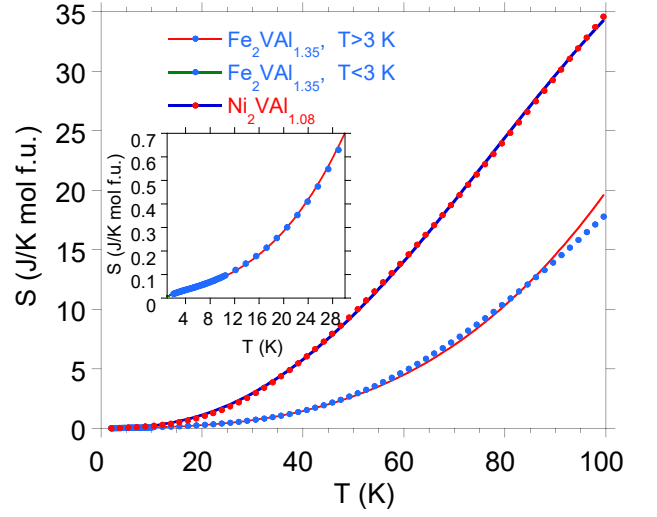


FIG. 11. $\text{Ni}_2\text{VAl}_{1.08}$, the fit of Eq. (3) to entropy S (blue line). For $\text{Fe}_2\text{VAl}_{1.35}$ entropy is well approximated by expression $S(T) \sim \gamma_0 T + \beta T^3 + sT^n$ with exponent $n = 3/2$ for $T < 3$ K (green line) and $n = -2$ for $T > 3$ K (red line). The inset displays details.

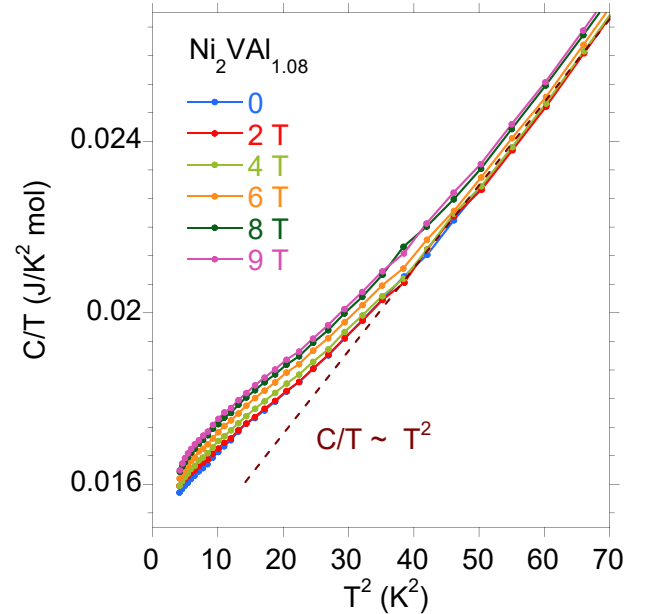


FIG. 12. Heat capacity C/T vs T^2 for $\text{Ni}_2\text{VAl}_{1.08}$ in magnetic fields. The linear C/T vs T^2 behavior is obeyed for temperatures $6 < T < 20$ K.

(a) shows κ , which is a sum of electronic (κ_e) and lattice (κ_L) contributions, measured between 2 and 350 K. In general, metals with higher Debye temperatures tend to have higher thermal conductivities. Therefore, one could expect a higher thermal conductivity for $\text{Fe}_2\text{VAl}_{1.35}$ than for its $\text{Ni}_2\text{VAl}_{1.08}$ analogue. $\text{Fe}_2\text{VAl}_{1.35}$ seems to be, however, an exception to this rule due to the presence of the pseudogap formed at the Fermi level due to interband hybridization, sample off-stoichiometry, and larger con-

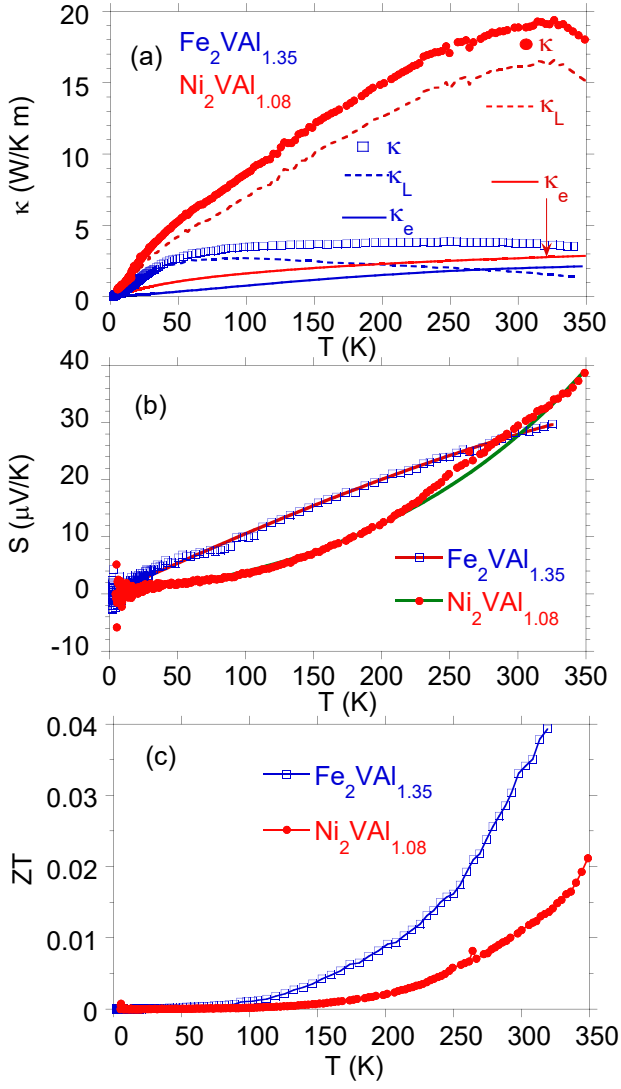


FIG. 13. Temperature variation of thermal conductivity κ (a), Seebeck coefficient S (b), and figure of merit ZT (c) of Fe₂VAI_{1.35} (blue open squares) and for Ni₂VAI_{1.08} (red points). Panel (a) also shows lattice (dotted line) and electronic (solid line) thermal conductivity for Fe₂VAI_{1.35} (blue) and Ni₂VAI_{1.08} (red), respectively. Panel (b) shows the fit of the SF model (Eq. 4) to the $S(T)$ data for Fe₂VAI_{1.35} (red solid line) and Ni₂VAI_{1.08} (blue solid line). The experimental data of Ni₂VAI_{1.08} deviate from the fit around ~ 270 K (broad maximum).

centration of its antisite defects, all of which contribute to lowering the thermal conductivity of Fe₂VAI_{1.35} in respect to κ of metallic Ni₂VAI sample.

The electronic thermal conductivity was evaluated using the Wiedemann-Franz law: $\kappa_e \rho / T = L_0$, where ρ is the measured dc electrical resistivity and $L_0 = 2.45 \times 10^{-8} \text{ W}\Omega\text{K}^{-2}$ is the Lorenz number, while κ_L was obtained by subtracting κ_e from the measured κ . The temperature dependencies of κ_L and κ_e shown in Fig. 13(a) are typical of disordered crystalline materials where phonon scattering by defects and grain boundaries

dominates.

As shown in Fig. 13(b), Seebeck coefficient S obtained for Ni₂VAI_{1.08} is approximated by Eq. 4, which expresses the temperature dependence of $S_{SF}(T)$ for nearly ferromagnetic, spin fluctuating metals [63] such as YCo₂ [64], under the condition that their susceptibility $\chi(T)$ shows a broad maximum (cf. Fig. 6),

$$S_{SF} = \tilde{\alpha}T + \tilde{\beta}T \left(\frac{T}{\tilde{T}_0} \right) \log \frac{\tilde{\delta} + (T/\tilde{T}_0)^2}{(T/\tilde{T}_0)^2}. \quad (4)$$

Within this modeling, d electrons are responsible for the spin fluctuation, while transport properties are due to conduction electrons, which are dragged by spin fluctuations (SF), $\tilde{\alpha}$, $\tilde{\beta}$, $\tilde{\delta}$, and \tilde{T}_0 are fitting parameters. The fitting procedure gives $\tilde{\alpha} = 0.029 \mu\text{V K}^{-2}$, $\tilde{\beta} = 0.053 \mu\text{V K}^{-2}$, $\tilde{T}_0 = 220$ K, and $\tilde{\delta} = 4.3$ for Ni₂VAI_{1.08}. The experimental data for $S(T)$ of Fe₂VAI_{1.35} can also be approximated by expression (4) with the fitting parameters $\tilde{\alpha} = 0.108 \mu\text{V K}^{-2}$, $\tilde{\beta} = -0.021 \mu\text{V K}^{-2}$, $\tilde{T}_0 = 300$ K, and $\tilde{\delta} = 4$. Nonetheless, spin fluctuations do not significantly enhance the value of figure of merit, ZT , which for the both alloys is about 10^{-2} at 350 K, as shown in Fig. 13(c).

In Fig. 14 we present the resistivity ρ of Fe₂VAI_{1.35} at different magnetic fields. The $\rho(T)$ data deviates from those, usually reported for stoichiometric Fe₂VAI compound [40, 65] and exhibit a semiconducting-like behavior, similar to that, reported for Fe₂TiSn [66, 67] and its alloys [57]. Between ~ 100 and 10 K $\rho \sim -\ln T$, which is

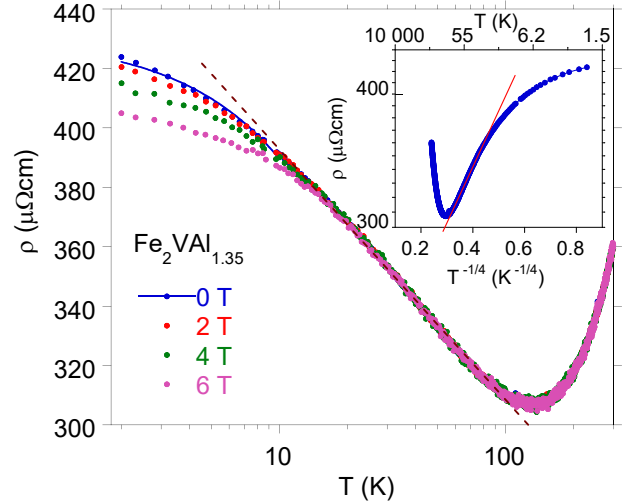


FIG. 14. Resistivity vs. temperature ($\ln T$ scale) of Fe₂VAI_{1.35} in magnetic fields up to 6 T. The dashed line indicates the $\ln T$ behavior in $\rho(T)$. The expression $\rho(T) = \rho_0 + bT^5 + c \ln(\mu/T) + \rho_{vrh} \exp(T_0/T)^{1/4} + r_{SG} T^{3/2}$ fits the $\rho(T, B = 0)$ data between 2 and 100 K (blue line), where the respective parts are the phonon, Kondo, Mott-VRH, and spin-glass contributions to the resistivity. The inset shows $\ln \rho$ vs. $T^{-1/4}$, with the linear change of ρ marked by the red line.

usually characteristic of Kondo behavior, whereas a sig-

nificant deviation from linearity is observed below 10 K. However, we note that within this low- T range there is observed a complex glassy-like phase, which complicates the interpretation of the ρ -data. Moreover, for $30 < T < 100$ K conductivity follows $\sigma = \sigma_{vrh} \exp[-(T_0/T)^{1/4}]$ (see Fig. 14, inset), which is typical for Mott variable-range hopping (VRH) behavior in three dimensions [68, 69]. Here T_0 characterizes the pseudogap at the Fermi level in the case of solids, where a conduction and valence band overlap giving a finite density of states $DOS(\epsilon_F)$ (see Sec. IV). With increasing overlap of the bands, mostly the d -electron states become delocalized, which can lead to a metal-insulator transition of Anderson type. In the limit of weak localization, conduction by hopping (VRH) could be possible, this is a case of the Fe sample. T_0 inversely depends on the localization length $\xi_L = [\frac{1}{18}DOS(\epsilon_F)k_B T_0]^{-1/3}$, which diverges at the insulator-metal transition [70]. The best approximation of $\rho = \rho_{vrh} \exp[(T_0/T)^{1/4}]$ to the experimental data shown in Fig. 14 gives $\rho_{vrh} = 208.7 \mu\Omega\text{cm}$ and $T_0 = 2.3$ K. Then, the localization length $\xi_L \approx 260 \text{ \AA}$ for $DOS(\epsilon_F) = 1.078 \text{ states/eV}$ (cf. Table III) is quite large, indicating direct proximity to the insulator-metal transition. Due to the above, we suggest that the hopping between Anderson-localized states is possible. Very recently, a similar conclusion was presented for stoichiometric Fe_2VAI [62].

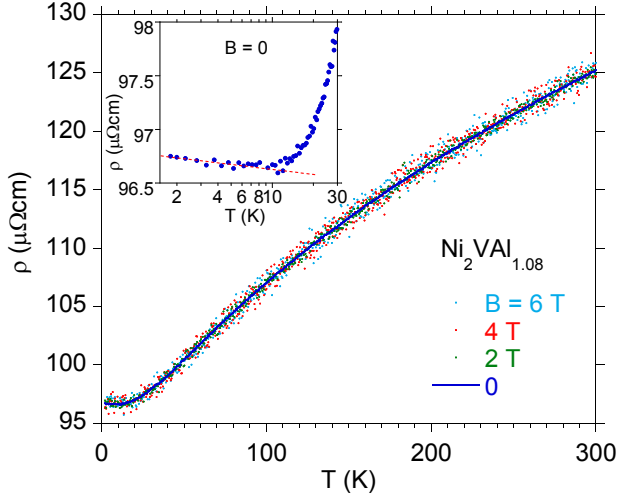


FIG. 15. Resistivity of $\text{Ni}_2\text{VAI}_{1.08}$ vs temperature in applied magnetic fields. In applied magnetic fields ρ vs T is measured with chaotic distribution of the experimental points with respect to the curvature of $\rho(T)$ for zero field. This chaotic spread of experimental points increases with increasing B . The inset shows a Kondo impurity behavior $\rho \sim -\ln T$.

The electrical transport of $\text{Fe}_2\text{VAI}_{1.35}$ reflects its complex interband and magnetic interactions; therefore, the resistivity of this alloy is discussed in relation to the paramagnetic $\text{Ni}_2\text{VAI}_{1.08}$. Figure 15 displays the resistivity of $\text{Ni}_2\text{VAI}_{1.08}$ as a function of temperature and in various magnetic fields. The $\rho(T)$ shown in the figure is almost not field-dependent. What is interesting, at the

lowest temperatures $\rho \sim -\ln T$, suggesting the scattering mechanism of conduction electrons due to the presence of magnetic Ni impurities (Kondo impurity effect).

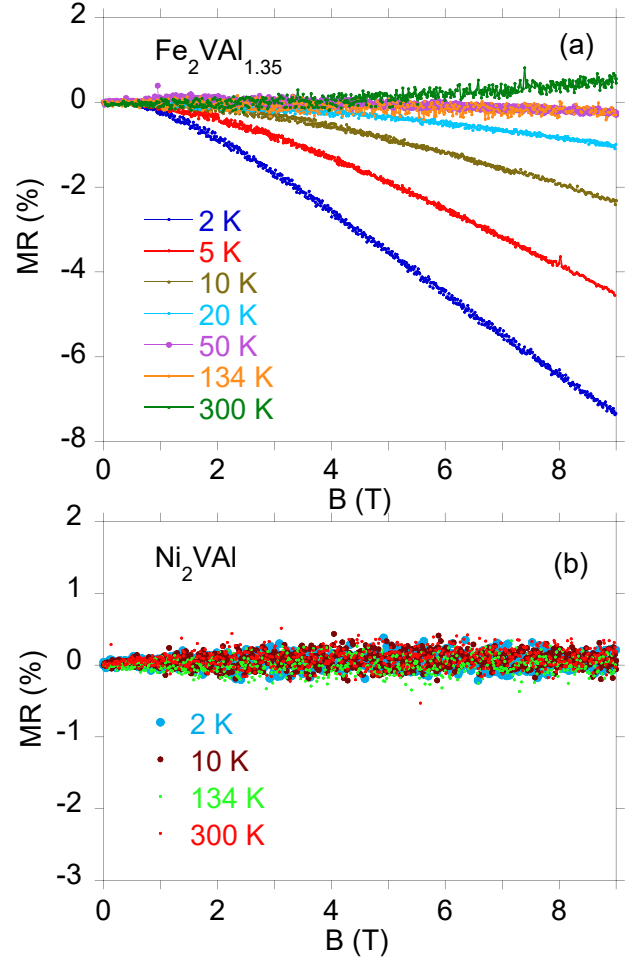


FIG. 16. (a) Magnetoresistance $MR = [\rho(B) - \rho(B = 0)]/\rho(B = 0) \times 100\%$ ($I = 5 \text{ mA}$), of $\text{Fe}_2\text{VAI}_{1.35}$ (a) and $\text{Ni}_2\text{VAI}_{1.08}$ (b) as a function of the magnetic field B , measured at several temperatures.

Figure 16 compares magnetoresistance isotherms, MR , of $\text{Fe}_2\text{VAI}_{1.35}$ (a) and $\text{Ni}_2\text{VAI}_{1.08}$ (b) measured from 0–9 T. MR is defined as $MR = [\rho(B) - \rho(B = 0)]/\rho(B = 0) \times 100\%$, where $\rho(B)$ and $\rho(0)$ are resistivities measured at $B=0$ and H T, respectively. Since the applied magnetic field suppresses fluctuations in magnetic moments and spin-dependent scattering, a possible source of negative MR can be Kondo behavior, as shown in Fig. 16(a). The MR isotherms of $\text{Fe}_2\text{VAI}_{1.35}$ were found to be negative, supporting the Kondo effect as the significant mechanism governing the low- T electrical phenomena. Remarkably, as shown in Fig. 17 the MR isotherms taken can be projected onto a single curve by plotting the MR data as a function of $B/(T + T^*)$, where T^* K is the characteristic temperature, usually considered as an approximate measure of the Kondo temperature [71]. The Schlottmann-type scaling was applied to $\text{Fe}_2\text{VAI}_{1.35}$

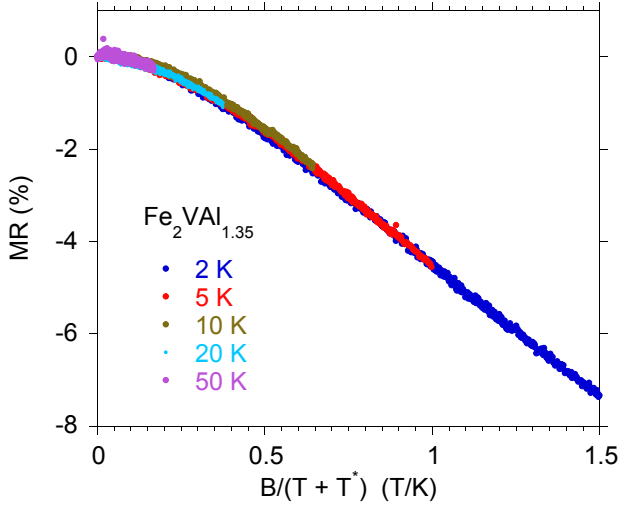


FIG. 17. Schlottmann-type plot of the magnetoresistance isotherms from panel Fig. 16(a). $T^* = 2.9$ K.

giving $T^* = 2.9$ K. The MR isotherms of $Ni_2VAI_{1.08}$ are quite different, MR does not exhibit any field dependence as shown in Fig. 16(b) (cf. Fig. 15), even though Ni magnetic impurities contribute a term to the electrical resistivity that increases logarithmically on temperature as temperature T is lowered. Maybe, the strongly diluted magnetic impurities give a weak effect, weaker than the spread of points on MR isotherms.

IV. EFFECT OF OFF-STOICHIOMETRY AND SITE DISORDER ON THE ELECTRONIC PROPERTIES OF $Fe_2VAI_{1+\delta}$ WITHIN DFT CALCULATIONS, COMPARISON WITH STOICHIOMETRIC Fe_2VAI AND Ni_2VAI

The electronic structure calculations for Fe_2VAI have shown that this compound is nonmagnetic and semi-metallic [11]. The calculated density of states of Fe_2VAI exhibits the 0.5 eV wide pseudogap located symmetrically around the Fermi level, as shown in Fig. 18(a). However, the electronic structure of this compound seems to be more interesting when Fe_2VAI is disordered or is off-stoichiometric. In the disordered $Fe_{2+x}V_{1-x}Al$ composition the Fe and V atoms at the antisite positions ($F \leftrightarrow V$) give rise to a narrow impurity d band located just in the middle of the quasi-gap calculated for an ordered Fe_2VAI compound [72]. This narrow d band formed by the antisite Fe defects can significantly change the shape of the valence band XPS spectra of disordered alloy, especially near the Fermi level, as shown in Fig. 19. Appearance of this strongly correlated d -like band was also reported for similar Fe_2TiSn compound due to an excess of Fe_{AS} atoms at Ti antisite positions [17]. The DOS of this narrow peak in the gap of the Fe_2TiSn bands is composed mainly of the $d - e_g$ states of Fe_{AS} that hybridize with the d states of the eight nearest Fe atoms in octahedral

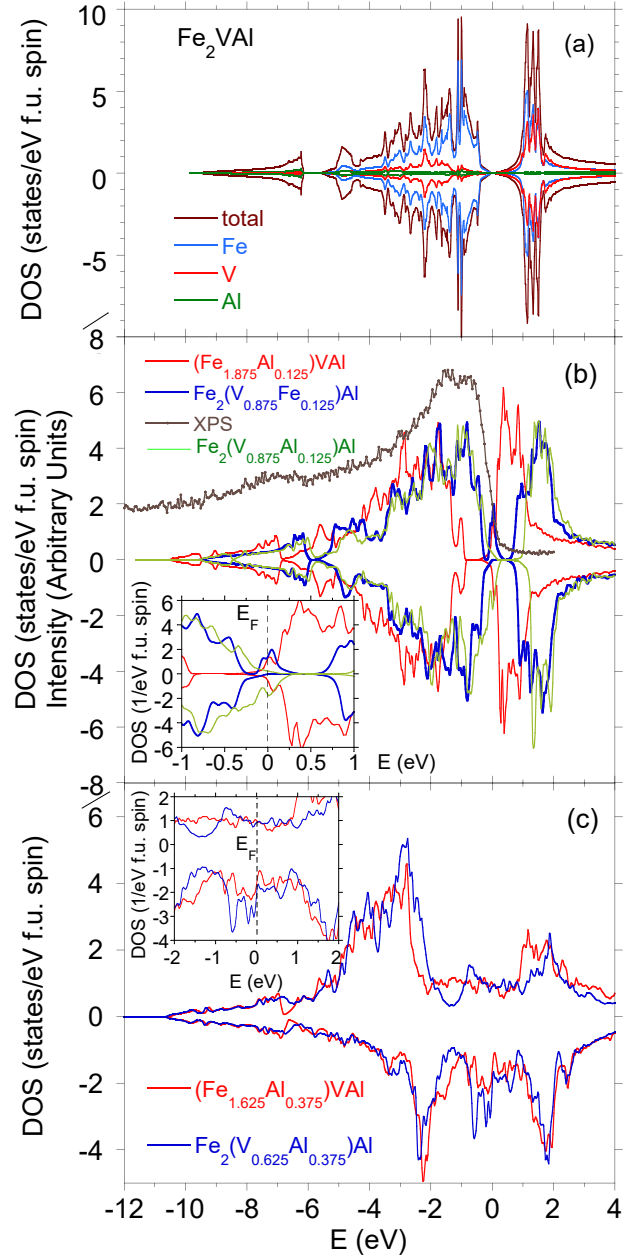


FIG. 18. (a) Calculated total and spin-resolved density of states (TDOS) within the LSDA+ U +SO ($U = 3$ eV) approximation for Fe_2VAI . Also are shown the partial TDOS calculated for Fe, V, and Al. (b) Valence band (VB) XPS spectrum for $Fe_2VAI_{1.35}$ (gray points) compared to the calculated TDOS (LSDA+ U +SO, $U = 3$ eV) for the supercell of various off-stoichiometry variants of Fe_2VAI . (c) The spin resolved TDOS within the LSDA+ U +SO, $U = 3$ eV, for $(Fe_{13}Al_3)V_8Al_8$ (red) and $Fe_{16}(V_5Al_3)Al_8$ (blue) supercells. The insets exhibit details near the Fermi level in an extended energy scale.

coordination; moreover, the calculated magnetic structure of $[Fe_{15}Ti_{AS}][Ti_7Fe_{AS}]Sn_8$ is of a cluster character (more details in Ref. [57]).

The narrow d -band of Fe_{AS} is a reason of sev-

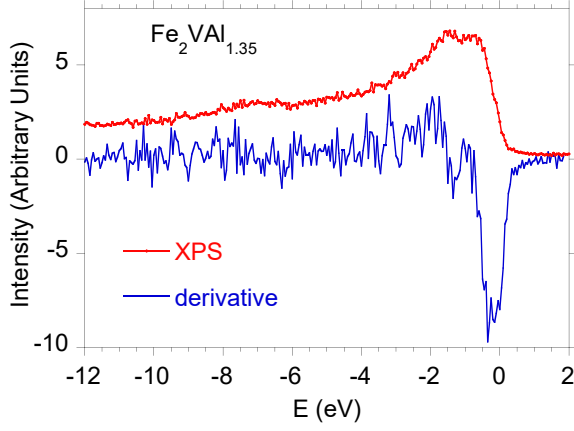


FIG. 19. Valence band XPS spectrum for $\text{Fe}_2\text{VAI}_{1.35}$ (red points) and its derivative dI/dE (blue line). The extreme in dI/dE for $E \approx 0.2$ eV is related to Fe_{AS} d -electron states located in the electronic bands near the Fermi level.

eral anomalous thermodynamic properties attributed to many-body effects. For example, the mechanism of electrical transport in Fe_2TiSn with AS Fe defects has been explained as a result of interband transitions between this narrow d band and other conduction states through a small gap at ϵ_F [57]. Here, we calculated the bands for Fe_2VAI and Ni_2VAI in various variants of their stoichiometry and in the presence of the AS structural disorder. One notes, $\text{Fe}_2\text{VAI}_{1.35}$ exhibits analogous $\rho(T)$ behavior to that of Fe_2TiSn , which suggests similar in nature electronic band properties of both the compounds.

The calculations were performed with the use of the FP-LAPW method complemented with local orbitals. The spin-orbit (SO) interaction for valence and local orbital states was taken into account, and the effective Hubbard parameter U_{eff} for the d -states of Fe, Ni, and V was assumed to be 3 eV. The super-cell methodology of alloy modeling was used to simulate the disorder. Figure 18 compares the atomic DOSs per atom for Fe_2VAI (a) with similar DOSs calculated for supercell of the off-stoichiometric Fe_2VAI analogues containing an excess of one Al atom located at Fe sites, $(\text{Fe}_{15}\text{Al}_1)\text{V}_8\text{Al}_8$, excess of one Fe at V sites, $\text{Fe}_{16}(\text{V}_7\text{Fe}_1)\text{Al}_8$, and excess of Al at V sites, $\text{Fe}_{16}(\text{V}_7\text{Al}_1)\text{Al}_8$, respectively (b), and off-stoichiometric analogues shown in panel (c) where three Al atoms are at Fe sites, $(\text{Fe}_{13}\text{Al}_3)\text{V}_8\text{Al}_8$, and three Al atoms occupy V sites, $\text{Fe}_{16}(\text{V}_5\text{Al}_3)\text{Al}_8$. The first variant of disorder with one atom at the AS position predicts the gap located in the electronic bands of the assumed compounds; however, its location with respect to ϵ_F is different depending on the atom at the AS site. Namely, when an Al atom occupies the Fe sites, the gap is located at energies $E < \epsilon_F$, for one Fe at V sites the gap is symmetrically located around ϵ_F , while for scenario with one Al at V sites the gap is located just above ϵ_F . All scenarios give narrow band states at ϵ_F , and are possible in the off-stoichiometry sample. However, note that only the AS Fe defects at V positions lead to the ap-

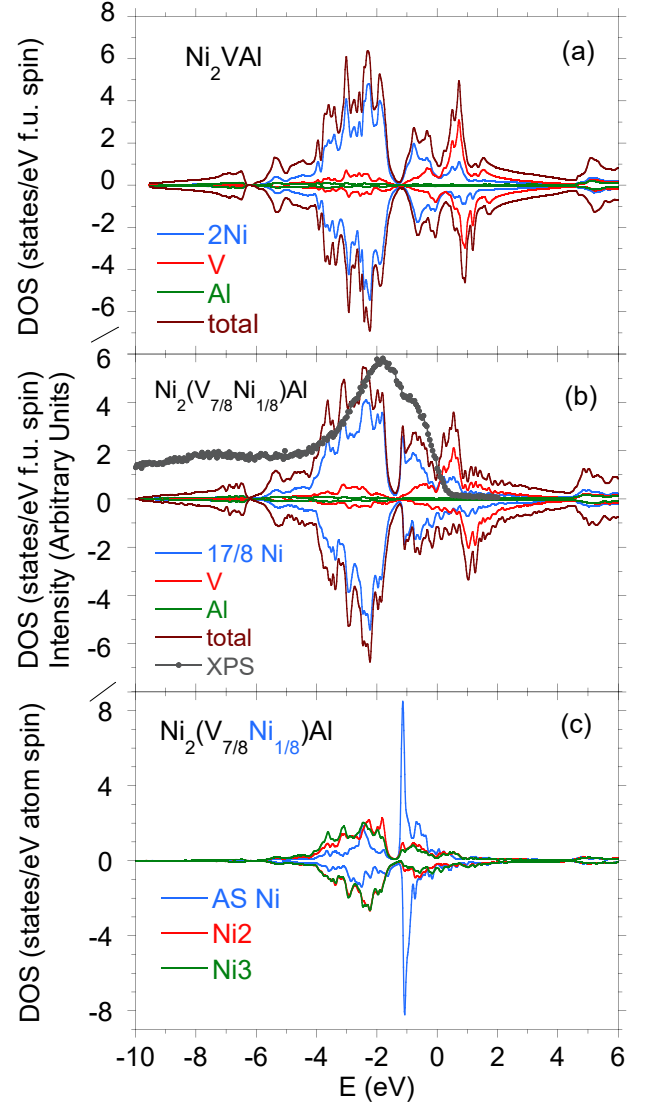


FIG. 20. (a) Calculated total and spin resolved DOS within the LSDA+ U +SO ($U = 3$ eV) for Ni_2VAI . Also are shown the partial TDOS calculated for Ni, V, and Al. (b) VB XPS spectrum for $\text{Ni}_2\text{VAI}_{1.08}$ (gray points) compared to the calculated TDOS (LSDA+ U +SO, $U = 3$ eV) for $\text{Ni}_{16}(\text{V}_7\text{Ni}_1)\text{Al}_8$ supercell. (c) Total DOS per one atom for Ni at various sites. The blue line represents the TDOS of AS Ni defects at V sites.

pearance of a narrow $3d \uparrow$ band at ϵ_F , which seems to be the most reasonable explanation for the experimental data shown in Fig. 14. Within this scenario, the VRH hopping through the pseudogap $k_B T_0$ of ~ 20 meV, which is calculated two orders in magnitude lower than the gap of Fe_2VAI , can be possible (cf. Fig. 18(b)). It is reasonable to assume that all three DOSs shown in panel (b) contribute to the total DOS of the disordered sample with appropriate weighting factors, with the result giving an agreement of calculations with the valence XPS spectra. The DOSs calculated for the more disordered system, with the exchange of three Al atoms with Fe or V assumed, respectively, do not give a good comparison

with the experiment, as shown in panel (c). The details of the DFT calculations are summarized in Table III.

Fig. 20 shows the valence band XPS spectra in comparison to the calculated total DOSs per formula for Ni_2VAl (a) and $\text{Ni}_{17}\text{V}_7\text{Al}_8$ supercell (b). This comparison clearly shows that the measured VB XPS spectra mostly reflect the $3d$ Ni and $3d$ V electronic states located between the Fermi energy and the binding energy 6 eV. The Al $3ps$ states are located between 6 and 10 eV below ϵ_F . One can note that the Ni AS defects do not drastically change the total DOSs of Ni_2VAl , however, they significantly contribute to the sharp d -electronic states at 1 eV below ϵ_F [in panel (c)], giving a magnetic moment of $0.14 \mu_B$ on Ni at AS positions (cf. Table IV). A localized magnetic moment calculated for AS Ni correlates well with the $\rho \sim -\ln T$ behavior, characteristic of the diluted Kondo systems (as shown in Fig. 15). Fi-

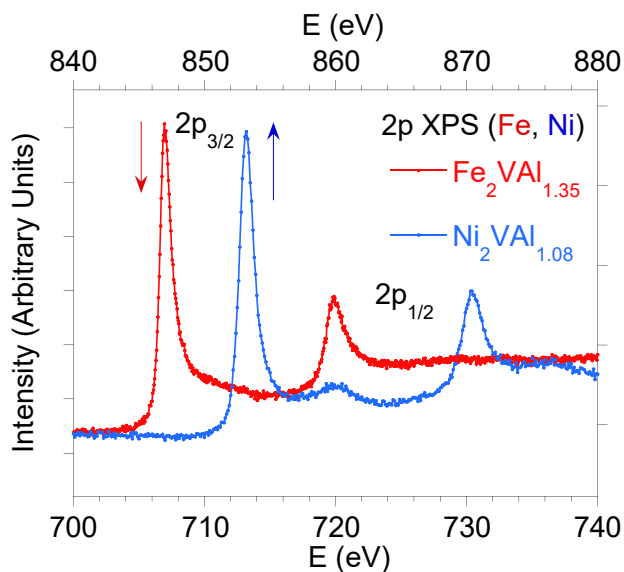


FIG. 21. $2p$ XPS core level spectra for Fe in $\text{Fe}_2\text{VAl}_{1.35}$ (red) and Ni in $\text{Ni}_2\text{VAl}_{1.08}$ (blue).

nally, we have measured the core level $2p$ XPS spectra for Fe in $\text{Fe}_2\text{VAl}_{1.35}$ and Ni in $\text{Ni}_2\text{VAl}_{1.08}$ to indirectly argue the low average magnetic moment of Fe and Ni in these compounds. The $2p$ XPS spectra are interpreted in reference to Refs. [73, 74], where for Mn-based Heusler alloys, it has been documented that the exchange splitting of the $2p_{3/2}$ level is directly correlated with the value of local magnetic moment at the Mn site. Specifically, the $2p_{3/2}$ splitting energy ΔE plotted as ΔE versus magnetic moment μ_{Mn} of Mn for a series of various Mn-based Heusler alloys exhibits a universal linear dependence, which gives for $\mu_{Mn} \sim 3 \mu_B$ a value of $\Delta E \sim 1$ eV. This experimental observation seems to be universal, and characteristic of other d -electron elements with localized magnetic moment larger than $2 \mu_B/\text{atom}$ (cf. Ref. [75]), simultaneously the XP spectroscopy allows one to quickly demonstrate the strength of μ . The $2p_{3/2}$ lines shown in Fig. 21 do not exhibit any ΔE splitting,

which suggests a nonmagnetic ground state or strongly delocalized d -electronic states or both, or that the magnetic moment localized on Fe and Ni, respectively, is not large enough to observe the splitting.

V. CONCLUDING REMARKS

Spin fluctuations in itinerant electron systems could give predominant effects on the thermodynamic properties of weakly or nearly ferromagnetic metals [42]. In consequence of the appearance of spin fluctuations, one expects an enhance of electronic specific heat, Pauli susceptibility, as well as a strong enhance of the thermopower. For many reasons, the disordered Fe_2VAl has been a candidate for good thermoelectric properties. In several previously published papers, the thermoelectric properties have been studied, either experimentally and theoretically [5, 41, 76] for pure Fe_2VAl and with dopants, however, the effect did not meet expectations. We investigated the off-stoichiometric $\text{Fe}_2\text{VAl}_{1.35}$ with excess of Al, however, the sample is not appropriate for thermoelectric applications. However, the sample is extremely interesting because of the complex magnetic properties caused by disorder. We documented the impact of AS disorder on the appearance of magnetic moment on Fe in AS positions, which in consequence leads to appearance of Griffiths phase state below $T_G \approx 200$ K, and singular properties in low-temperature susceptibility. In the paramagnetic regime inverse susceptibility of $\text{Fe}_2\text{VAl}_{1.35}$ obeys the Curie-Weiss law, while below a characteristic temperature T_G $1/\chi$ displays a downward deviation from the CW law with evidently field dependent behavior, indicating the onset of short-range ferromagnetic correlation well above T_C^g , which is considered a hallmark of Griffiths singularity.

The DFT calculations were carried out for the disordered Fe_2VAl and its off-stoichiometric variants. The *ab initio* calculations predicted the Fe_2VAl compound to be *nonmagnetic* narrow-gap semiconductor, while for similar disordered and/or off-stoichiometric alloys Fe occupying the AS V sites is always calculated magnetic. Both band structure calculations and magnetic measurements showed at most one AS Fe defect per unit cell; therefore, the system can be treated as dilute. In result, the Griffiths phase state is possible in such a diluted system due to the finite probability of randomly large, pure, and differently diluted clusters. This result allowed us to simulate the magnetization versus temperature within the Ising model in an external magnetic field, in good agreement with the experimental data shown in Fig. 3.

The physical properties of $\text{Fe}_2\text{VAl}_{1.35}$ are analyzed with respect to paramagnetic Ni_2VAl . Up to now, this compound has not been sufficiently well investigated, more of its possible behaviors have been predicted from DFT calculations [77–80]. We present comprehensive thermodynamic investigations as well as transport properties for this compound. Our DFT calculations pre-

TABLE III. Fe₂VAl ($Fm\bar{3}m$) and the off-stoichiometric analogues; FP-LAPW results for supercell of (Fe₁₅Al₁)V₈Al₈, Fe₁₆(V₇Fe₁)Al₈, and Fe₁₆(V₇Al₁)Al₈. n_l is a number of valence electrons, $l = 0, 1, 2,$ and 3 ($s, p, d,$ and f electron states, respectively). m is total magnetic moment of each atom in the supercell.

supercell	formula unit	m_{total} (μ_B /f.u.)	DOS(ϵ_F) (1/eV f.u.)	γ_0^{calc} (mJ/K ² mol)		
	Fe ₂ VAl	0	0	0		
atom	multiplicity	n_s	n_p	n_d	n_f	$m_{total}/atom$ in μ_B
Al	1	2.4354	6.5068	0.1094	0.0120	0.000
Fe	2	2.2332	6.1952	5.8200	0.0070	0.000
V	1	2.1458	6.0268	2.4886	0.0152	0.000
Fe ₁₅ V ₈ Al ₉	(Fe _{15/8} Al _{1/8})VAl	0.04	1.93	4.55		
atom	multiplicity	n_s	n_p	n_d	n_f	$m_{total}/atom$ in μ_B
Fe1	1	2.24	6.20	5.83	0.01	0.155
Fe2	1	2.24	6.20	5.83	0.01	0.082
Fe3	1	2.23	6.19	5.82	0.01	-0.123
Fe4	4	2.23	6.19	5.82	0.01	-0.052
Fe5	2	2.23	6.19	5.82	0.01	-0.056
Fe6	4	2.23	6.19	5.81	0.01	0.012
Fe7	2	2.23	6.19	5.81	0.01	0.018
V1	4	2.15	6.03	2.46	0.01	0.056
V2	4	2.15	6.03	2.42	0.01	0.039
Al1	4	2.43	6.50	0.12	0.01	0.000
Al2	4	2.43	6.50	0.11	0.01	0.000
Al3	1	2.43	6.52	0.10	0.01	0.000
Fe ₁₆ V ₇ Al ₉	Fe ₂ (V _{7/8} Al _{1/8})Al	0.21	2.18	5.13		
atom	multiplicity	n_s	n_p	n_d	n_f	$m_{total}/atom$ in μ_B
Al1	2	2.4350	6.5119	0.1190	0.0121	-0.00574
Al2	4	2.4330	6.5040	0.1147	0.0117	-0.00542
Al3	2	2.4329	6.5037	0.1147	0.0118	-0.00509
Fe1	8	2.2284	6.1911	5.8335	0.0065	0.34381
Fe2	8	2.2332	6.1961	5.8190	0.0070	0.01825
Al4	1	2.4260	6.4748	0.1119	0.0111	-0.02047
V1	1	2.1520	6.0366	2.4217	0.0157	0.00161
V2	4	2.1508	6.0356	2.4231	0.0154	-0.16059
V3	2	2.1508	6.0357	2.4225	0.0154	-0.15168
Fe ₁₇ V ₇ Al ₈	Fe ₂ (V _{7/8} Fe _{1/8})Al	0.38	1.078	2.54		
atom	multiplicity	n_s	n_p	n_d	n_f	$m_{total}/atom$ in μ_B
Fe1	1	2.2377	6.1858	5.5736	0.0117	2.98449
Fe2	8	2.2261	6.1824	5.8144	0.0065	0.46897
Fe3	8	2.2292	6.1881	5.8108	0.0066	-0.41870
V1	4	2.1479	6.0294	2.4138	0.0142	-0.05980
V2	2	2.1479	6.0299	2.4149	0.0143	-0.04267
V3	1	2.1482	6.0304	2.4103	0.0145	0.29083
Al1	2	2.4315	6.4919	0.1079	0.0110	-0.00698
Al2	4	2.4317	6.4923	0.1086	0.0110	-0.00697
Al3	2	2.4300	6.4984	0.1122	0.0110	-0.00303

dict magnetic moment on Ni at AS V sites, which is a reason of appearance of Kondo diluted effect in the low-temperature resistivity of Ni₂VAl, however, the superconductivity demonstrated by *ab initio* calculations,

as was reported by Sreenivasa *et al.* [78], has not been confirmed experimentally for this compound.

TABLE IV. Ni₂VAl ($Fm\bar{3}m$) and the off-stoichiometric analogues; FP-LAPW results for supercell of Ni₁₆(V₇Ni₁)Al₈. n_l is a number of valence electrons, $l = 0, 1, 2,$ and 3 ($s, p, d,$ and f electron states, respectively). m is total magnetic moment of each atom in the supercell.

supercell	formula unit	m_{total} (μ_B /f.u.)	DOS(ϵ_F) (1/eV f.u.)	γ_0^{calc} (mJ/K ² mol)		
Ni ₂ VAl		0.335	3.06	7.22		
atom	multiplicity	n_s	n_p	n_d	n_f	m_{total}/atom in μ_B
Ni	2	2.2946	6.2264	7.9708	0.0051	0.00649
V	1	2.1273	6.0018	2.4359	0.0103	0.29991
Al	1	2.4171	6.4704	0.0835	0.0084	-0.00541
Ni ₁₇ V ₇ Al ₈ Ni ₂ (V _{7/8} Ni _{1/8})Al		0.38	2.361	5.57		
atom	multiplicity	n_s	n_p	n_d	n_f	m_{total}/atom in μ_B
Ni1	1	2.2244	6.1632	7.9765	0.0060	-0.01783
Ni2	8	2.2887	6.2181	7.9810	0.0055	-0.06997
Ni3	8	2.2896	6.2269	7.9605	0.0054	0.14194
V1	4	2.1293	6.0035	2.4393	0.0109	0.57564
V2	2	2.1293	6.0035	2.4417	0.0108	0.61413
V3	1	2.1294	5.9973	2.4440	0.0108	0.87389
Al1	2	2.4157	6.4562	0.0813	0.0083	-0.00698
Al2	4	2.4157	6.4564	0.0811	0.0083	-0.00753
Al3	2	2.4180	6.4798	0.0921	0.0093	-0.00782

Appendix A: Numerical analysis

In Sec. III A we argue that the deviation from the CW law is driven by the formation of ferromagnetic clusters. As discussed in Sec. IV, *ab initio* calculations indicate the presence of magnetic moments on wrong-site iron atoms. The divergence of susceptibility χ (cf. Fig. 2) suggests a ferromagnetic interaction between them. However, since down to the lowest temperatures studied, the system is in the paramagnetic state, those moments are too diluted to develop a ferromagnetic state. Moreover, as can be seen in Fig. 3a), $\chi(T)$ clearly deviates from the Curie law $\chi_C \propto T^{-1}$, which we attribute to magnetic clusters formed in the Griffiths phase. To support this assumption, we performed Monte Carlo simulations for small magnetic clusters to determine the temperature dependence of their contribution to the bulk magnetic susceptibility. We assume that the main signal comes from the bulk of the system and fulfills the Curie law, so determine the contribution from magnetic clusters, in Fig. 22a) we present the difference between the measured susceptibility χ and χ_C for different values of the magnetic field.

In Fig. 22b), for comparison, we present a temperature dependence of the magnetic susceptibility of a very small ($2 \times 2 \times 2$) cluster described by the Ising model in an external magnetic field. However, there are two differences between these two results. The first is related to the behavior at low temperatures. On the one hand, the measured susceptibility χ remains finite when $T \rightarrow 0$, while χ_C diverges as T^{-1} . Therefore, $\chi - \chi_C$ goes to $-\infty$ when $T \rightarrow 0$ (only $\chi > \chi_C$ is shown in Fig. 22a). On the other hand, the susceptibility χ_I of the Ising model goes to zero

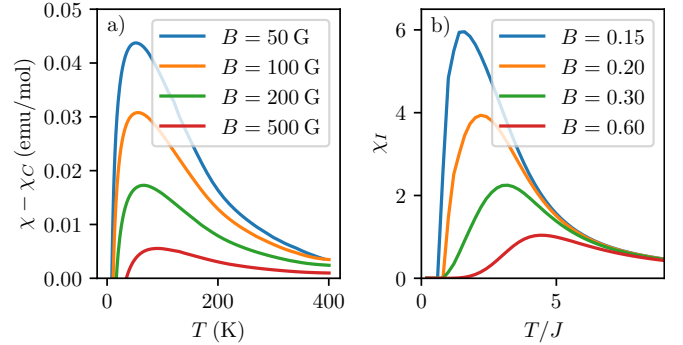


FIG. 22. a) Difference between the measured susceptibility $\chi(T)$ and susceptibility given by the Curie law χ_C . Only part for $\chi > \chi_C$ is shown. b) Magnetic susceptibility χ_I of a $2 \times 2 \times 2$ Ising model in external magnetic field.

when $T \rightarrow 0$. This discrepancy can result from approximations/limitations applied to $\chi - \chi_C$, e.g., instead of the Curie law, the bulk susceptibility can be described by the Curie-Weiss law with $\theta_{CW} < 0$ which does not have a singularity at $T = 0$. The other difference between panels a) and b) of Fig. 22 can be seen at high temperature, where χ_I is almost temperature independent, while $\chi - \chi_C$ decreases with increasing temperature. This discrepancy can result from neglecting other contributions to the magnetic susceptibility, e.g., the effect of spin fluctuations. The qualitative differences between the shapes of the lines are also due to the vast simplification of considering only one size of the clusters. In the Griffiths phase we expect an ensemble of clusters of different sizes

with their distribution depending on temperature. Moreover, we took into account the simplest possible kind of magnetic interactions in the cluster, i.e. the Ising model. This simplification does not allow for different magnetization orientations in different clusters, which is expected because of the complex nature of the RKKY interaction. However, the qualitative agreement of the temperature dependencies of $\chi - \chi_C$ and χ_I we observe despite the use of strong approximations applied both to $\chi - \chi_C$ and to the modeled χ_I is a strong argument for the presence

of magnetic clusters in the system.

*Author to whom correspondence should be addressed: andrzej.slebarski@us.edu.pl

ACKNOWLEDGMENTS

Numerical calculations have been carried out using High Performance Computing resources provided by the Wrocław Centre for Networking and Supercomputing.

-
- [1] C. Felser and A. Hirohata, *Heusler Alloys: Properties, Growth, Applications* (Springer International Publishing, 2016).
- [2] S. Chatterjee, S. Chatterjee, S. Giri, and S. Majumdar, *J. Phys.: Condens. Matter*, **34**, 013001 (2022).
- [3] T. Klimczuk, C. H. Wang, K. Gofryk, F. Ronning, J. Winterlik, G. H. Fecher, J. -C. Griveau, E. Colineau, C. Felser, J. D. Thompson, D. J. Safarik, and R. J. Cava, *Phys. Rev. B* **85**, 174505 (2012).
- [4] Z. Lin, E3S Web of Conferences **213**, 02016 (2020).
- [5] D. Bourgault, H. Hajoum, S. Pairis, O. Leynaud, R. Haettel, J. F. Motte, O. Rouleau, and E. Alleno, *ACS Appl. Energy Mater.* **6**, 1526 (2023); and references cited therein.
- [6] K. Sato, T. Naka, M. Taguchi, T. Nakane, F. Ishikawa, Y. Yamada, Y. Takaesu, T. Nakama, A. deVisser, and A. Matsushita, *Phys. Rev. B* **82**, 104408 (2010).
- [7] A. Ślebarski and J. Goraus, *Phys. Rev. B* **80**, 235121 (2009).
- [8] T. Naka, K. Sato, M. Taguchi, T. Nakane, F. Ishikawa, Y. Yamada, Y. Takaesu, T. Nakama, and A. Matsushita, *Phys. Rev. B* **85**, 085130 (2012).
- [9] T. Naka, A. M. Nikitin, Yu Pan, A. de Visser, T. Nakane, F. Ishikawa, Y. Yamada, M. Imai, and A. Matsushita, *J. Phys.: Condensed Matter*, **28**, 285601 (2016).
- [10] R. Weht and W. E. Pickett, *Phys. Rev. B* **58**, 6855 (1998).
- [11] D. J. Singh and I. I. Mazin, *Phys. Rev. B* **57**, 14352 (1998).
- [12] G. Y. Guo, G. A. Botton, and Y. Nishino, *J. Phys.: Condens. Matter*, **10**, L199 (1998).
- [13] T. Graf, C. Felser, and S. S. Parkin, *Prog. Solid State Chem.* **39**, 1 (2011).
- [14] I. Galanakis, P. H. Dederichs, and N. Papanikolaou, *Phys. Rev. B* **66**, 174429 (2002).
- [15] Y. Nishino, H. Kato, M. Kato, and U. Mizutani, *Phys. Rev. B* **63**, 233303 (2001).
- [16] A. Matsushita, T. Naka, Y. Takano, T. Takeuchi, T. Shishido, and Y. Yamada, *Phys. Rev. B* **65**, 075204 (2002).
- [17] A. Ślebarski, *J. Phys. D: Appl. Phys.* **39**, 856 (2006).
- [18] R. B. Griffiths, *Phys. Rev. Lett.* **23**, 17 (1969).
- [19] Griffiths observed a nonanalytic behavior of the magnetization above Curie temperature T_c in a randomly diluted Ising ferromagnet, caused by the formation of ferromagnetic clusters above T_c [18]. This intermediate phase between the ferromagnetic and paramagnetic phases is referred to as the Griffiths phase.
- [20] F. S. da Rocha, G. L. F. Fraga, D. E. Brandão, c. M. da Silva, and A. A. Gomes, *Physica B* **269**, 154 (1999).
- [21] Z. Wen, Y. Zhao, H. Hou, B. Wang, and P. Han, *Materials and Design* **114**, 398 (2017).
- [22] Y-K Wang and J-Ch Tung, *Physics Open*, **2**, 100008 (2020).
- [23] P. V. Sreenivasa Reddy, V. Kanchana, G. Vaitheeswaran, and D. J. Singh, *J. Phys.: Condens. Matter* **28**, 115703 (2016).
- [24] J. Rodriguez-Carvajal, *Physica B* **192**, 55 (1993).
- [25] B. H. Toby, *Powder Diffr.* **21**, 67 (2006).
- [26] D. J. Singh, L. Nordstrom *Plane Waves, Pseudopotentials, and the LAPW Method* (2nd edition), Springer Science (2006), ISBN 978-0-387-28780-5.
- [27] P. Blaha, K. Schwarz, G. K. H. Madsen, D. Kvasnicka, and J. Luitz, *WIEN2k, An Augmented Plane Wave + Local Orbitals Program for Calculating Crystal Properties* (Karlheinz Schwarz, Techn. Universität Wien, Austria, 2001).
- [28] J. P. Perdew, K. Burke, and M. Ernzerhof, *Phys. Rev. Lett.* **77**, 3865 (1996).
- [29] V. I. Anisimov, J. Zaanen, and O. K. Andersen, *Phys. Rev. B* **44**, 943 (1991).
- [30] V. I. Anisimov, I. V. Solovyev, M. A. Korotin, M. T. Czyżyk, G. A. Sawatzky, *Phys. Rev. B* **48**, 16929 (1993).
- [31] V_2FeAl is a well known Pauli paramagnet, however, its magnetic properties sensitively depend on the degree of atomic order on the different crystallographic sites. The ground state of V_2FeAl , obtained experimentally and from the *ab-initio* calculations [32] is determined weakly magnetic for various structural models, which means that the disorder induces the short-range magnetic ordering below about 220 K.
- [32] R. Smith, Z. Gercsi, R. Zhang, K. E. Siewierska, K. Rode, and J. M. D. Coey, <https://arxiv.org/pdf/2309.11480v1.pdf>
- [33] S. Chatterjee1, S. Giri1, S. Majumdar, P. Dutta, P. Singha, and A. Banerjee, **34**, 295803 (2022).
- [34] A. Ślebarski, J. Goraus, and M. Fijałkowski, *Phys. Rev. B* **84**, 075154 (2011).
- [35] A. J. Bray, *Phys. Rev. Lett.* **59**, 586 (1987).
- [36] R. Shankar and G. Murthy, *Phys. Rev. B* **36**, 536 (1987).
- [37] M. Randeria, J. P. Sethna, and R. G. Palmer, *Phys. Rev. Lett.* **54**, 1321 (1985).
- [38] A. H. Castro Neto, G. Castilla, and B. A. Jones, *Phys. Rev. Lett.* **81**, 3531 (1998).
- [39] A. K. Pramanik and A. Banerjee, *Phys. Rev. B* **81**,024431 (2010).

- [40] Y. Nishino, M. Kato, S. Asano, K. Soda, M. Hayasaki, and U. Mizutani, *Phys. Rev. Lett.* **79**, 1909 (1997).
- [41] N. Tsujii, A. Nishide, J. Hayakawa, and T. Mori, *Sci. Adv.* **5**, 5935 (2019).
- [42] T. Moriya, *Spin Fluctuation in Itinerant Electron Magnetism* (Springer-Verlag, Berlin Heidelberg, 1985).
- [43] T. Takahashi, *Spin Fluctuation Theory of Itinerant Magnetism* (Springer-Verlag Berlin Heidelberg, 2013).
- [44] A. J. Cox, J. G. Loudereback, S. E. Apsel, and L. A. Bloomfield, *Phys. Rev. B* **49**, 12295 (1994).
- [45] M. Castro, C. Jamorski, and D. R. Salahub, *Chem. Phys. Lett.* **271**, 133 (1997).
- [46] Y. Jo, M. H. Jung, M. C. Kyum, K. H. Park, and Y. N. Kim, *J. Magnetism*, **11**, 156 (2006).
- [47] J. A. Mydosh, *Spin Glasses: An Experimental Introduction* (Taylor and Francis, London, 1993).
- [48] $n = 0$ corresponds to Debye-type exponential relaxation, for $n = 1$, there is no relaxation at all.
- [49] R. S. Freitas, L. Ghivelder, F. Damay, F. Dias, and L. F. Cohen, *Phys. Rev. B* **64**, 144404 (2001).
- [50] A. H. Castro Neto and B. A. Jones *Phys. Rev. B* **62**, 14975 (2000).
- [51] P. Levy, F. Parisi, L. Granja, E. Indelicato, and G. Polla, *Phys. Rev. Lett.* **89**, 137001 (2002).
- [52] S. Hari Krishnan, S. Rökler, C. M. N. Kumar, Y. Xiao, H. L. Bhat, U. K. Rökler, F. Steglich, S. Wirth, and S. Elizabeth, *J. Phys.: Condens. Matter* **22**, 346002 (2010).
- [53] A. Tari, *The Specific Heat of Matter at Low Temperatures*, Imperial College Press, London 2003.
- [54] C.S. Lue, J.H. Ross, Jr, C.F. Chang and H.D. Yang, *Phys. Rev. B* **60**, R13941 (1999).
- [55] C.S. Lue, H.D. Yang, and Y.K. Kuo, *Chinese Journal of Physics* **43**, 775 (2005).
- [56] K. Ikeda, S. K. Dhar, M. Yoshizawa, and K. A. Gschneidner, Jr., *J. Magn. Magn. Mater.* **100**, 292 (1991).
- [57] A. Ślebarski, J. Deniszczyk, W. Borgiel, A. Jezierski, M. Swatek, A. Winiarska, M. B. Maple, and W. M. Yuhasz *Phys. Rev. B* **69**, 155118 (2004).
- [58] J. Spalek, *European J. Phys.* **21**, 511 (2000).
- [59] K. D. Schotte and U. Schotte, *Phys. Lett. A* **55**, 38 (1975).
- [60] H. -U. Desgranges and K. D. Schotte, *Phys. Lett. A* **91**, 240 (1982).
- [61] O. Trovarelli, J. G. Sereni, G. Schmerber, and J. P. Kappler, *Phys. Rev. B* **49**, 15179 (1994).
- [62] F. Garmroudi, M. Parzer, A. Riss, A. V. Ruban, S. Khmelevskiy, M. Reticciooli, M. Knopf, H. Michor, A. Pustogow, T. Mori, and E. Bauer, *Nature Communications* **13**, 3599 (2022).
- [63] T. Okabe, *J. Phys.: Condens. Matter* **22**, 115604 (2010).
- [64] E. Gratz, A. S. Markosyan, *J. Phys.: Condens. Matter* **13**, R385 (2001).
- [65] A. Ślebarski, J. Goraus, J. Deniszczyk, and Ł. Skoczeń, *J. Phys.: Condens. Matter* **18**, 10319 (2006).
- [66] A. Ślebarski, M. B. Maple, E. J. Freeman, C. Sirvent, D. Tworuzska, M. Orzechowska, A. Wrona, A. Jezierski, S. Chiuzbaian, and M. Neumann, *Phys. Rev. B* **62**, 3296 (2000).
- [67] S. Chaudhuri, P. A. Bhobe1, A. Bhattacharya, and A. K. Nigam, *J. Phys.: Condens. Matter* **31**, 045801 (2019).
- [68] N. F. Mott, *Phil. Mag.* **13**, 989 (1966).
- [69] N. F. Mott, *Metal-Insulator Transitions* (Taylor and Francis LTD, London, 1974).
- [70] J. Delahaye, J. P. Brison, and C. Berger, *Phys. Rev. Lett.* **81**, 4204 (1998).
- [71] P. Schlottmann, *Z. Phys. B: Condens. Matter* **51**, 223 (1983).
- [72] J. Deniszczyk, *Acta Phys. Pol. B* **32**, 529 (2001).
- [73] Yu. M. Yarmoshenko1, M. I. Katsnelson1, E. I. Shreder, E. Z. Kurmaev, A. Ślebarski, S. Plogmann, T. Schlathölter, J. Braun, and M. Neumann, *Eur. Phys. J. B* **2**, 1 (1998).
- [74] S. Plogmann, T. Schlathölter, J. Braun, M. Neumann, Yu. M. Yarmoshenko, M. V. Yablonskikh, E. I. Shreder, E. Z. Kurmaev, A. Wrona, and A. Ślebarski, *Phys. Rev. B* **60**, 6428 (1999).
- [75] A. Ślebarski, M. Neumann, and B. Schneider, *J. Phys.: Condens. Matter*, **13**, 5515 (2001).
- [76] G. A. Naydenov, P. J. Hasnip, V. K. Lazarov, and M. J. Probert, *J. Phys.: Condens Matter.* **32**, 125401 (2020).
- [77] F. S. da Rocha, G. L. F. Fraga, D. E. Brandão, C. M. da Silva, and A. A. Gomes, *Physica B* **269**, 154 (1999).
- [78] P. V. S. Reddy, V. Kanchana, G. Veitheswaran, and D. J. Singh, *J. Phys.: Condens Matter.* **28**, 115703 (2016).
- [79] Z. Wen, Y. Zhao, H. Hou, B. Wang, and P. Han, *Materials and Design*, **114**, 398 (2017).
- [80] Y. -K. Wang and J. -Ch. Tung, *Physics Open* **2**, 100008 (2020).